

REPORT DOCUMENTATION PAGE					Form Approved OMB No. 0704-0188	
<small>The public reporting burden for this collection of information is estimated to average 1 hour per response, including the time for reviewing instructions, searching existing data sources, gathering and maintaining the data needed, and completing and reviewing the collection of information. Send comments regarding this burden estimate or any other aspect of this collection of information, including suggestions for reducing the burden, to Department of Defense, Washington Headquarters Services, Directorate for Information Operations and Reports (0704-0188), 1215 Jefferson Davis Highway, Suite 1204, Arlington, VA 22202-4302. Respondents should be aware that notwithstanding any other provision of law, no person shall be subject to any penalty for failing to comply with a collection of information if it does not display a currently valid OMB control number.</small> PLEASE DO NOT RETURN YOUR FORM TO THE ABOVE ADDRESS.						
1. REPORT DATE (DD-MM-YYYY) 03/28/2013		2. REPORT TYPE Final Technical Report			3. DATES COVERED (From - To) 01/06/2010 - 12/31/2012	
4. TITLE AND SUBTITLE Planar Solid-Oxide Fuel Cell Research and Development				5a. CONTRACT NUMBER		
				5b. GRANT NUMBER N00014-10-1-0462		
				5c. PROGRAM ELEMENT NUMBER		
6. AUTHOR(S) Dr. Sagar Kapadia Dr. W. Kyle Anderson Dr. James Newman Mr. Bruce Hilbert				5d. PROJECT NUMBER		
				5e. TASK NUMBER		
				5f. WORK UNIT NUMBER		
7. PERFORMING ORGANIZATION NAME(S) AND ADDRESS(ES) The University of Tennessee 615 McCallie Avenue Chattanooga, TN 37403-2504					8. PERFORMING ORGANIZATION REPORT NUMBER	
9. SPONSORING/MONITORING AGENCY NAME(S) AND ADDRESS(ES) Office of Naval Research 875 North Randolph Street Arlington, VA 22203-1995					10. SPONSOR/MONITOR'S ACRONYM(S)	
					11. SPONSOR/MONITOR'S REPORT NUMBER(S)	
12. DISTRIBUTION/AVAILABILITY STATEMENT Approved for Public Release; distribution is unlimited						
13. SUPPLEMENTARY NOTES						
14. ABSTRACT Numerical simulation capabilities to perform flowfield analysis and sensitivity analysis of solid oxide fuel cells (SOFCs) have been developed. A three-dimensional, implicit, multi-species fuel cell solver is modified to analyze cell geometries supplied by NexTech Materials (NexTech). Four different NexTech cell configurations of varying complexities have been analyzed in this study. A capability to perform thermo-mechanical analysis of NexTech cells is developed by coupling the fuel cell code with the structures code. The capability was initially developed for a simplified cell that also included sensitivity analysis of thermo-mechanical variables. Sensitivity derivatives are computed using the direct differentiation method in the fuel cell and structures codes.						
15. SUBJECT TERMS						
16. SECURITY CLASSIFICATION OF:			17. LIMITATION OF ABSTRACT	18. NUMBER OF PAGES	19a. NAME OF RESPONSIBLE PERSON	
a. REPORT	b. ABSTRACT	c. THIS PAGE			19b. TELEPHONE NUMBER (Include area code) (423) 425 5497	

INSTRUCTIONS FOR COMPLETING SF 298

1. REPORT DATE. Full publication date, including day, month, if available. Must cite at least the year and be Year 2000 compliant, e.g. 30-06-1998; xx-06-1998; xx-xx-1998.

2. REPORT TYPE. State the type of report, such as final, technical, interim, memorandum, master's thesis, progress, quarterly, research, special, group study, etc.

3. DATES COVERED. Indicate the time during which the work was performed and the report was written, e.g., Jun 1997 - Jun 1998; 1-10 Jun 1996; May - Nov 1998; Nov 1998.

4. TITLE. Enter title and subtitle with volume number and part number, if applicable. On classified documents, enter the title classification in parentheses.

5a. CONTRACT NUMBER. Enter all contract numbers as they appear in the report, e.g. F33615-86-C-5169.

5b. GRANT NUMBER. Enter all grant numbers as they appear in the report, e.g. AFOSR-82-1234.

5c. PROGRAM ELEMENT NUMBER. Enter all program element numbers as they appear in the report, e.g. 61101A.

5d. PROJECT NUMBER. Enter all project numbers as they appear in the report, e.g. 1F665702D1257; ILIR.

5e. TASK NUMBER. Enter all task numbers as they appear in the report, e.g. 05; RF0330201; T4112.

5f. WORK UNIT NUMBER. Enter all work unit numbers as they appear in the report, e.g. 001; AFAPL30480105.

6. AUTHOR(S). Enter name(s) of person(s) responsible for writing the report, performing the research, or credited with the content of the report. The form of entry is the last name, first name, middle initial, and additional qualifiers separated by commas, e.g. Smith, Richard, J, Jr.

7. PERFORMING ORGANIZATION NAME(S) AND ADDRESS(ES). Self-explanatory.

8. PERFORMING ORGANIZATION REPORT NUMBER. Enter all unique alphanumeric report numbers assigned by the performing organization, e.g. BRL-1234; AFWL-TR-85-4017-Vol-21-PT-2.

9. SPONSORING/MONITORING AGENCY NAME(S) AND ADDRESS(ES). Enter the name and address of the organization(s) financially responsible for and monitoring the work.

10. SPONSOR/MONITOR'S ACRONYM(S). Enter, if available, e.g. BRL, ARDEC, NADC.

11. SPONSOR/MONITOR'S REPORT NUMBER(S). Enter report number as assigned by the sponsoring/monitoring agency, if available, e.g. BRL-TR-829; -215.

12. DISTRIBUTION/AVAILABILITY STATEMENT. Use agency-mandated availability statements to indicate the public availability or distribution limitations of the report. If additional limitations/ restrictions or special markings are indicated, follow agency authorization procedures, e.g. RD/FRD, PROPIN, ITAR, etc. Include copyright information.

13. SUPPLEMENTARY NOTES. Enter information not included elsewhere such as: prepared in cooperation with; translation of; report supersedes; old edition number, etc.

14. ABSTRACT. A brief (approximately 200 words) factual summary of the most significant information.

15. SUBJECT TERMS. Key words or phrases identifying major concepts in the report.

16. SECURITY CLASSIFICATION. Enter security classification in accordance with security classification regulations, e.g. U, C, S, etc. If this form contains classified information, stamp classification level on the top and bottom of this page.

17. LIMITATION OF ABSTRACT. This block must be completed to assign a distribution limitation to the abstract. Enter UU (Unclassified Unlimited) or SAR (Same as Report). An entry in this block is necessary if the abstract is to be limited.

Planar Solid-Oxide Fuel Cell Research and Development

S. Kapadia, W. K. Anderson, J. Newman, B. Hilbert

University of Tennessee SimCenter at Chattanooga,
701, East M.L. King Boulevard, Chattanooga, TN – 37403, U.S.A.

Abstract

Numerical simulation capabilities to perform flowfield analysis and sensitivity analysis of solid oxide fuel cells (SOFCs) have been developed. A three-dimensional, implicit, multi-species fuel cell solver is modified to analyze cell geometries supplied by NexTech Materials (NexTech). Four different NexTech cell configurations of varying complexities have been analyzed in this study. A capability to perform thermo-mechanical analysis of NexTech cells is developed by coupling the fuel cell code with the structures code. The capability was initially developed for a simplified cell that also included sensitivity analysis of thermo-mechanical variables. Sensitivity derivatives are computed using the direct differentiation method in the fuel cell and structures codes.

1. Introduction

Development of alternative energy producing devices has attracted a lot of attention from researchers all over the world in recent years. Due to its capability of producing efficient energy using various hydrocarbon fuel types, Solid Oxide Fuel Cells (SOFCs) present a promising technology for the future. Even though SOFCs are still in the developmental stage, numerical techniques can be effectively utilized to find solutions to many of the design hurdles affecting the commercial application of the technology. Experimental and numerical approaches have been undertaken by several researchers [1-8] to study the behavior of SOFC. Some of the advantages of the numerical simulations over the experiments are the cost effectiveness and the fact that the simulations provide a wealth of data that is difficult or impossible to obtain experimentally and can be used to perform in-depth analysis of the SOFC unit/system. Numerical simulations can contribute greatly toward the development of better designs that can produce more power, increased efficiency, and extended life expectancy of various SOFC components.

To date, numerical simulations have been primarily focused on analysis of fuel cells or fuel cell components, without strong emphasis on utilizing the simulations in a design optimization environment. Because of the emphasis on analysis instead of design, sensitivity information to determine the effects of variations in design parameters on performance has been primarily implemented by simply changing the parameter of interest, re-running the simulation, and comparing the results with those from the original simulation [1,5-6,8]. While this approach can be used to determine the effects of parameter variations on fuel cell performance, a more rigorous approach toward

optimization would likely lead to better designs, and can also provide improved insight into the parameters affecting the performance of the fuel cell. For SOFC problems, example cost functions that can be used for improving performance include minimizing temperature variations, obtaining equal distribution of fuel in each of the channels, minimizing stress inside different components or maximizing power. Design variables may be related to the shape/size of the fuel channels, electrodes, electrolyte, and interconnect, but may also be coupled to the stoichiometric composition of fuel or material properties such as the porosity or tortuosity of the electrodes.

In references [9] and [10], optimization algorithms have been used to improve the performance of a polymer-electrolyte-membrane fuel cell (PEM) using four design variables, where the sensitivity derivatives used for the optimization algorithm have been obtained using a finite-difference approach. While finite differences are often a viable means for computing sensitivity derivatives, this method can be computationally restrictive when a sufficiently large number of design variables are present. In addition, accurate derivatives can sometimes be difficult to obtain using finite differences because of subtractive cancellation errors [11], which occur when the function evaluations in the numerator become computationally indistinguishable [12] when very small perturbations are used. By using a direct differentiation or discrete adjoint method [16-27], sensitivity derivatives that are consistent with the flow solver may be obtained for use in a design optimization environment. The fuel cell code utilized in this report is capable of computing sensitivity derivatives of a cost function with respect to desired parameters using both direct differentiation and discrete adjoint methods. Although sensitivity studies shown in this report uses direct differentiation method to compute sensitivity derivatives, implementation and verification of discrete adjoint method in the fuel cell code has been published in previous work [28-31]. In different design studies performed at the SimCenter, sensitivity derivatives were also utilized in a design environment to optimize cost functions representing uniform fuel distribution [28,31], temperature distribution [29] and cell voltage [31].

Due to the presence of various thermal mechanisms inside SOFC, temperature distribution exhibits non-uniformity throughout the domain. This coupled with the mismatch in coefficients of thermal expansion of different SOFC components makes stress analysis an interesting avenue to explore. Recently, few studies have been performed [32-38] to analyze stress components inside different components of SOFC. Lin et al. [32] analyzed effects of clamping load on the thermal stress distribution in a planar SOFC. Five different compressible loads were applied to investigate effects on stress distribution. Gulfam et al. [35] analyzed thermal stress inside PEN region of SOFC for co-flow, counter-flow and cross-flow configurations using commercial software, ABAQUS [39]. Maximum stress inside anode layer was found at high-temperature regions located on the anode-electrolyte interface for all configurations. Jiang et al. [36] performed thermal stress analysis of SOFC with the bonded compliant seal design. Stress analysis performed using commercial software, FLUENT [40] and ANSYS [41] investigated effects of temperature non-uniformity and cell voltage on thermal stress distribution. Weil and Koeppel [37] also

analyzed effects of different seal designs on stress-strain state. They used glass-ceramic, brazed joints and foil-based seals in this study. Chiang et al. [38] analyzed effects of anode porosity on thermal stress in anode-supported SOFC using commercial software, STAR-CD [42] and MARC [43]. The study indicated presence of higher principal stress at low cell voltages due to high local current density and steep temperature gradients.

None of the studies mentioned in the previous paragraph attempted to compute sensitivity derivatives of a cost function involving thermal stress components using formal procedures such as direct differentiation or discrete adjoint methods. Such capability is required if optimization of principal stress components or strain rates with respect to geometrical or material parameters is desired. One of the cases (Case 5) described in this report demonstrates such capability, where stress sensitivities are computed with respect to the cathode porosity. Implementation of this method is not trivial, as it requires computation of sensitivity derivatives of flowfield variables in the fuel cell code and coupling them with the structures solver to compute stress sensitivities with respect to the design parameters.

The primary goal of this report is to describe results (Case 1 – Case 4) of simulations performed on different NexTech cell configurations. Also, development of fluid-structure interaction capability to analyze thermal stress distribution (Case 4, Case 5) and stress sensitivities (Case 5) in different components of SOFC is described. The results presented in Case 1 deals with the FlexCell, which contains honeycomb electrolyte. The fuel cell code required several modifications to analyze this unconventional geometry. The cell used in the second case (Case 2) can be termed as a simple fluid cell. Cell components included in this simulation are fuel manifold, current collector and interconnect. Primary purpose of this analysis was to compare results obtained using the SimCenter code with the numerical results obtained by the NexTech personnel. The third geometry (Case 3) obtained from NexTech was a 28mm cell that included all relevant components. However, while the grid was being generated on this cell, it was decided through mutual discussion to shift focus to the more important G13 cell. A thorough analysis on G13 cell (Case 4) has been performed that also includes stress analysis. Finally, results obtained on a simplified SOFC cell have been shown in Case 5. This geometry was utilized to develop initial fluid-structure interaction capability to perform stress analysis. This case also demonstrates the capability to compute sensitivity derivatives of structural cost functions.

2. Solution Methodology

2.1 Governing Equations (Fuel Cell)

The three-dimensional SOFC model [30,31] utilized in this report solves the multi-species Navier-Stokes equations along with an electric potential equation that governs the distribution of electric potential and current density in the field. The three-dimensional model accounts for all components of the SOFC, including the anode, cathode, electrolyte, current collectors, seals, interconnects, and the fuel and air channels. Note that the model

is not limited to any particular type of SOFC, i.e. planar as well as tubular type SOFC can be simulated using this model.

The governing equations for mass, momentum and energy conservation are solved simultaneously with the equation governing the electric potential in the numerical model. The system of equations utilized in the model is given by equations (1) - (6), which represent the conservation statements for the species concentrations, momentum (x, y and z), energy and current, respectively.

Equations (1) – (5) are modified Navier-Stokes equations valid for both porous and fluid regions. Detailed discussion on flux formulation for these equations can be found in previous work [28-31]. Equation (6) represents the electric potential equation. As solid regions are considered zero-velocity regions, only energy (interconnect, electrolyte, seals) and electric potential equations (interconnect, electrolyte) are solved inside them. Electric/ionic conductivity, σ , in equation (6) is a strong function of the temperature. Expressions describing the relationships between the electric/ionic resistivity (reciprocal of conductivity) and the temperature for various components of SOFC are presented in Table 1 [44,45] along with thermal conductivities and other material properties of different components of the SOFC.

$$\frac{\partial(\varepsilon\rho_i)}{\partial t} + \nabla \cdot (\varepsilon\rho_i \vec{V}) + \nabla \cdot (\vec{J}_i) = S_i \quad (1)$$

$$\frac{\partial(\varepsilon\rho u)}{\partial t} + \nabla \cdot (\varepsilon\rho u \vec{V}) = -\varepsilon \frac{\partial P}{\partial x} + \nabla \cdot (\varepsilon\tau_x) - \frac{\varepsilon^2 u \mu}{B} \quad (2)$$

$$\frac{\partial(\varepsilon\rho v)}{\partial t} + \nabla \cdot (\varepsilon\rho v \vec{V}) = -\varepsilon \frac{\partial P}{\partial y} + \nabla \cdot (\varepsilon\tau_y) - \frac{\varepsilon^2 v \mu}{B} \quad (3)$$

$$\frac{\partial(\varepsilon\rho w)}{\partial t} + \nabla \cdot (\varepsilon\rho w \vec{V}) = -\varepsilon \frac{\partial P}{\partial z} + \nabla \cdot (\varepsilon\tau_z) - \frac{\varepsilon^2 w \mu}{B} \quad (4)$$

$$\frac{\partial(\varepsilon E_t)}{\partial t} + \nabla \cdot (\varepsilon(E_t + P)\vec{V}) + \nabla \cdot (\sum_{ns} \vec{J}_i H_i) = \nabla \cdot (\varepsilon\mu\tau\vec{V}) - \nabla \cdot \vec{q}^{eff} + \nabla \phi \cdot (\sigma \nabla \phi) \quad (5)$$

$$\nabla \cdot (\sigma \nabla \phi) = 0 \quad (6)$$

As presented, equation (6) is an elliptic equation contrary to the rest of the governing equations, which are hyperbolic-parabolic equations. Equation (6) is solved in the entire domain except for the fuel and air channels, which are pure fluid regions.

Several transport processes take place at the anode-electrolyte and the cathode-electrolyte interfaces that strongly affect the overall behavior of the SOFC. The electrochemical reactions taking place at the cathode-electrolyte and anode-electrolyte interfaces can be described by equations (7) and (8), respectively.



Table 1. Material properties of various components of SOFC [44, 45]	
Electric resistivity of anode (Ωm)	$2.98 \times 10^{-5} \exp(-1392 / T)$
Electric resistivity of cathode (Ωm)	$8.11 \times 10^{-5} \exp(600 / T)$
Electric resistivity of interconnect (Ωm)	6.41×10^{-8}
Ionic resistivity of electrolyte (Ωm)	$2.94 \times 10^{-5} \exp(10350 / T)$
Thermal conductivity of anode ($W m^{-1} K^{-1}$)	40.0
Thermal conductivity of anode current collector ($W m^{-1} K^{-1}$)	11.0
Thermal conductivity of cathode ($W m^{-1} K^{-1}$)	10.0
Thermal conductivity of cathode current collector ($W m^{-1} K^{-1}$)	11.0
Thermal conductivity of interconnect ($W m^{-1} K^{-1}$)	25.0
Thermal conductivity of electrolyte ($W m^{-1} K^{-1}$)	2.0
Thermal conductivity of seals ($W m^{-1} K^{-1}$)	1.5
Porosity of anode	0.6
Porosity of cathode	0.6
Tortuosity of anode	6.0
Tortuosity of cathode	6.0
Porosity of anode current collector	0.9
Porosity of cathode collector	0.9
Tortuosity of anode collector	1.5
Tortuosity of cathode collector	1.5

The effect of the aforementioned electrochemical reactions is modeled by applying mass flux conditions at the cathode-electrolyte (equation (9)) and anode-electrolyte (equations (10)-(11)) interfaces using Faraday's law.

$$J_{O_2} = -\frac{i}{4F} M_{O_2} \quad (9)$$

$$J_{H_2} = -\frac{i}{2F} M_{H_2} \quad (10)$$

$$J_{H_2O} = \frac{i}{2F} M_{H_2O} \quad (11)$$

In the above equations, i is the local current density and F is Faraday's constant. A negative sign implies that the flux is leaving the interface.

To account for the heat generated due to electrochemistry, heat flux proportional to the entropy change associated with the electrochemical reaction is applied at the anode-electrolyte and cathode-electrolyte interfaces. This heat flux is proportional to the molar formation rate, $(i / n_e F)$, where n_e is the number of electrons participating in the electrochemical reaction.

In addition to the electrochemical reactions, two chemical reactions, methane reforming (12.1) and water gas shift (12.2) reactions have been included inside the anode for Case 5. For other SOFC cases (Case 1, Case 4), the fuel mixture contains only two species, hydrogen and steam and thus, only electrochemical reactions described by equations (7) – (8) are included in the model.



Reaction rates for various species have been computed using the following equations.

$$Rate_r = kf_r p_{CH_4} p_{H_2O} - kb_r p_{CO} p_{H_2}^3 \quad (13.1)$$

$$Rate_s = kf_s p_{CO} p_{H_2O} - kb_s p_{CO_2} p_{H_2} \quad (13.2)$$

Subscripts “ r ” and “ s ” stand for reforming and shift reactions, respectively. Reaction rate constants, kf and kb , are computed using the methodology outlined in reference [29].

The voltage output of the SOFC strongly depends on several irreversibilities or losses encountered in the flowfield including activation polarization, concentration polarization and Ohmic polarization. Noren and Hoffman [46] have provided extensive discussion on accurately modeling the activation polarization. The SOFC model used in this work employs the Butler-Volmer equation to compute activation polarization [46].

The Butler-Volmer equation can be written as,

$$i = i_0 \left[\exp \left(\alpha \frac{n_e F}{R_u T} \eta_{act} \right) - \exp \left((1 - \alpha) \frac{n_e F}{R_u T} \eta_{act} \right) \right] \quad (14)$$

The activation polarization is denoted by η_{act} .

α is the charge transfer coefficient and assumed to be 0.5 in the current work.

n_e represents the number of electrons involved in the electrochemical reaction, which is 2 (equations (7) and (8)) in the current simulation.

i_0 is the exchange current density and is computed using equations (15) and (16) for the anode and cathode [47], respectively.

$$i_{0,a} = \zeta_a \left(\frac{P_{H_2}}{P_{ref}} \right) \left(\frac{P_{H_2O}}{P_{ref}} \right) \exp \left(- \frac{E_{act,a}}{R_u T} \right) \quad (15)$$

$$i_{0,c} = \zeta_c \left(\frac{P_{O_2}}{P_{ref}} \right)^{0.25} \exp \left(- \frac{E_{act,c}}{R_u T} \right) \quad (16)$$

Various constants in the above equations are given in Table 2 [47]. Once the values of α and n_e are inserted in equation (14), the activation polarization can be computed using the following expression.

$$\eta_{act} = \left(\frac{R_u T}{F} \right) \sinh^{-1} \left(\frac{i}{2i_0} \right) \quad (17)$$

Table 2. Constants used to compute activation polarization [47]	
α	0.5
n_e	2
$\zeta_a (A m^{-2})$	5.5×10^8
$\zeta_c (A m^{-2})$	7.0×10^8
$E_{act,a} (J kmol^{-1})$	1.0×10^8
$E_{act,c} (J kmol^{-1})$	1.2×10^8
$P_{ref} (N m^{-2})$	101325

Ohmic polarization is a direct consequence of the resistance offered to the flow of electrons/ions inside various components of the SOFC. Voltage drop due to Ohmic resistance is directly proportional to the current and the resistance. The effect of Ohmic

polarization on the voltage loss is directly included in the potential equation, equation (6), through the electric conductivity, σ , which is the reciprocal of the electric resistivity.

Concentration polarization is caused by reductions in the concentrations of the reacting species at the interface between the electrodes and the electrolyte. The effect of the reduction in concentrations can be seen from the well-known Nernst potential equation, given by equation (18). Also, exchange current densities at the anode-electrolyte interface and the cathode-electrolyte interface, represented by equations (15) and (16), respectively, are strongly affected by the concentration polarization.

Equation (18) computes the electromotive force (EMF) or electric potential under reversible conditions, i.e. in the absence of activation, Ohmic or any other losses.

$$EMF = EMF^0 + \frac{RT}{2F} \ln \left(\frac{\bar{P}_{H_2} \bar{P}_{O_2}^{0.5}}{\bar{P}_{H_2O}} \right), \text{ where } \bar{P}_i = \frac{P_i}{P_{ref}} \quad (18)$$

The electromotive force at standard pressure, EMF^0 , is computed using polynomial thermodynamic relationship between Gibbs free energy and temperature of different species participating in the electrochemical reactions. The value of P_{ref} is taken as one atmosphere in the above equation.

The electrochemical reaction reduces the concentration of the reactants and increases the concentration of the products at the electrode-electrolyte interface. Thus, the partial pressures of the reactants and products are affected in the same manner. This will reduce the value of the second term on the right-hand side of the equation (18) thereby affecting the EMF of the cell adversely. Concentration polarization strongly depends on the material properties of the electrodes that are responsible for the transport (diffusion and convection) of the reactants and products, to and from the electrode-electrolyte interface.

2.2 Governing Equations and Computational Methodology (Structure)

2.2.1 Governing Equations (Structure)

As mentioned earlier, capability to perform thermo-mechanical stress analysis has been developed to analyze stress inside different components of the SOFC. Thermo-mechanical stress analysis can be performed either fully coupled, or one-way coupled in which only one disciplinary response affects the other. Regardless of the formulation, the governing equation may be expressed as

$$\sigma_{ij,i} + b_j = \rho \frac{\partial^2 u_j}{\partial t^2} \quad (19)$$

where, σ represents the stress tensor, b the body force terms per unit mass, ρ the mass density, and u the displacement field. To cast the above equations in terms of displacements, the relationships between strain-displacement and stress-strain must be

assumed. For small strains and displacements (i.e., geometric linearity), the strains are related to the deformation gradients as

$$\varepsilon_{ij} = \frac{1}{2}(u_{j,i} + u_{i,j}) \quad (20)$$

Additionally, under the assumption of linear elasticity (i.e. material linearity), the stress may be related to strain as

$$\sigma_{ij} = C_{ijkl}(\varepsilon_{kl} - \alpha \cdot \Delta T \cdot \delta_{kl}) \quad (21)$$

where, α is the coefficient of thermal expansion (which may in general be a function of temperature), ΔT the temperature difference from reference, and δ the Kronecker delta symbol. Here, the first term relates the stress to mechanical strain, and the second to the thermal strain. Assuming isotropic material behavior, the constitutive (elasticity) tensor may be conveniently written as

$$C_{ijkl} = \frac{E}{2(1+\nu)}(\delta_{il}\delta_{jk} + \delta_{ik}\delta_{jl}) + \frac{E\nu}{(1+\nu)(1-2\nu)}\delta_{ij}\delta_{kl} \quad (22)$$

where, in general, the modulus of elasticity, E , and Poisson's ratio, ν , may be functions of temperature. Currently, it is assumed that the mechanical response does not alter the temperature distribution, and therefore, a one-way coupling is utilized. Furthermore, a steady-state temperature field is applied to the structure and, hence, inertia may be neglected in the problem formulation.

2.2.2 Computational Methodology (Structure)

The thermo-elastic structural analysis is performed using a standard displacement-based Galerkin formulation. With introduction of the stress-strain, and strain-displacement, relations into the equations of equilibrium, the Navier-displacement equations may be written (neglecting inertia) as

$$C_{ijkl}u_{k,li} + b_j = 0 \quad (23)$$

Integrating these equations over the volume of an element, using a standard Galerkin formulation, and assembling the element equations yields an algebraic system to be solved for the unknown nodal displacement vector $\{d\}$ as

$$[K]\{d\} = \{F\} \quad (24)$$

where, the global stiffness matrix and load vector are

$$[K] = \sum \int [B]^T [C] [B] dV \quad (25)$$

$$\{F\} = \sum \int [N]^T \{b\} dV + \sum \int [N]^T \{t\} dS + \sum \int [N]^T [C] \{\alpha \cdot \Delta T\} dV \quad (26)$$

Here, $[N]$ represents the element shape function matrix, which relates the displacement field to the element nodal displacements, and $[B]$ is the so-called strain-

displacement matrix, which relates the element strains to the nodal displacements. The first term of the load vector represents body forces acting over the volume of the domain, the second term represents forces due to traction or stress ($t_i = \sigma_{ij}\eta_j$, where η_j are the components of the unit outward pointing normal) acting on the boundaries of the domain, whereas the last term are the loads resulting from the thermal strains.

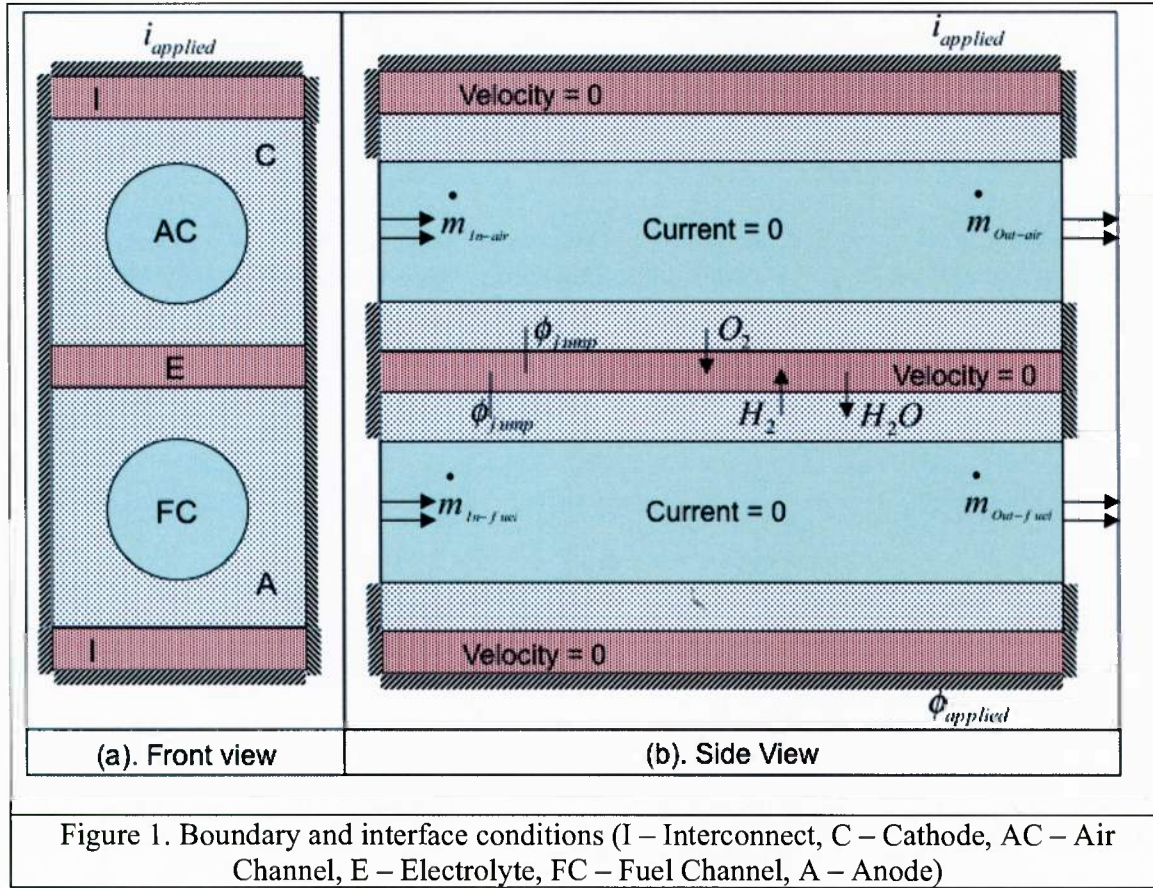
The solution to the resulting system may be accomplished with either an iterative or direct method. Iterative solution algorithms can be beneficial for very large systems which may prohibit direct solution methods, or for systems which do not have symmetric damping matrices. The direct method uses a sparse Cholesky decomposition based on skyline storage scheme. A preconditioned GMRES [48] is utilized to solve the system iteratively.

Once the nodal displacements have been determined, the strain and stress fields may be computed. In multidimensional problems, the individual components of the stress tensor do not provide adequate information in order to ascertain the proximity to failure or yielding of the material. In these regards, different stress measures are typically used. For brittle materials, the maximum in plane principal stress is typically used. The principal planes are those in which the shear stress vanishes and, therefore, are the planes that have maximum normal stress. Since brittle materials tend to fail due to normal stress, appropriate failure criteria are usually based on maximum principal stress. For ductile materials, which tend to fail in shear, typically either the von Mises or the Tresca yield criteria are used. The von Mises yield criterion uses the assumption that the onset of yield is based on the second deviatoric stress invariant. The Tresca yield surface is circumscribed by the von Mises yield surface, representing a more conservative criterion for prediction of plastic yielding.

2.3 Boundary Conditions

Boundary conditions utilized in the numerical solver are described for a sample geometry shown in Figure 1. The geometry includes all relevant SOFC components including air/fuel channels, anode, cathode, electrolyte and interconnects. No-slip, adiabatic wall boundary conditions are applied at the interfaces between the electrodes and the interconnect, as well as the side, top and bottom walls. Solid regions (interconnect and electrolyte) are considered zero-velocity regions and the only variables computed inside these regions are temperature and electric potential. A fixed potential ($\phi = 0$) boundary condition is applied at the bottom wall, whereas the top wall is treated by specifying average current density ($i = i_{\text{applied}}$).

Inflow boundary conditions with specified mass flow rate and species mole fractions are applied at both fuel and air channel inlets. Specified back pressure outflow conditions are applied at both air and fuel channel outlets.



2.4 Sensitivity Analysis - Direct Differentiation

As mentioned earlier, direct differentiation method is utilized in both the fuel cell and structures codes to compute sensitivity derivatives. Derivation of this method using the chain rule is shown in equations (27) – (30). Q represents the vector of solution variables where each element of the vector is representative of one or more physical variables located at each mesh point, χ . R represents the vector of discrete residuals at each mesh point, f is the cost function and β is a vector of design variables.

$$\frac{df(Q(\beta), \chi(\beta), \beta)}{d\beta} = \frac{\partial f}{\partial \beta} + \frac{\partial f}{\partial Q} \frac{\partial Q}{\partial \beta} + \frac{\partial f}{\partial \chi} \frac{\partial \chi}{\partial \beta} \quad (27)$$

$$\text{Now, } R(Q(\beta), \chi(\beta), \beta) = 0 \quad (28)$$

$$\Rightarrow \frac{dR}{d\beta} = \frac{\partial R}{\partial \beta} + \frac{\partial R}{\partial Q} \frac{\partial Q}{\partial \beta} + \frac{\partial R}{\partial \chi} \frac{\partial \chi}{\partial \beta} = 0 \quad (29)$$

$$\Rightarrow \left[\frac{\partial R}{\partial Q} \right] \left\{ \frac{\partial Q}{\partial \beta} \right\} = - \left\{ \frac{\partial R}{\partial \beta} \right\} - \frac{\partial R}{\partial \chi} \frac{\partial \chi}{\partial \beta} \quad (30)$$

As seen, computation of $\partial Q / \partial \beta$ is an essential component of this method, which requires the solution of a linear system of equations for each design variable. This requirement makes direct differentiation methods computationally expensive for problems with many design variables. Discrete adjoint method is more favorable for the problems involving large number of design variables. However, as derivatives of dependent variables with respect to the design variables are computed at each node in the flowfield in direct differentiation, this method is particularly useful when there are many flowfield constraints.

2.5 Solution Procedure

Flowfield variables are computed using an unstructured, implicit, finite-volume solver. The solver is vertex centered and the discrete residual at each node is computed by integrating the governing equations, (1) – (6) over a median dual control volume. Because a steady-state solution is the primary goal of the current work, time accuracy of the solution is sacrificed by allowing local time-stepping to accelerate convergence.

To reduce computer time, the solution is obtained using multiple processors utilizing the message passing interface (MPI) [49] and necessary grid decomposition is achieved using METIS [50]. Original grids are generated using the commercial software Pointwise [51].

An implicit Euler scheme is used to solve the non-linear system as given by equations (1) - (6). A flux-difference splitting scheme based on the ROE scheme [52,53] for a multi-component mixture is derived to model the convective fluxes. A central-difference formulation is used to compute all the second-order derivative terms. Linear systems encountered in both the flowfield and sensitivity solvers are solved using the GMRES [48] method.

3. Results and Discussion

3.1 Analysis

3.1. Case 1 (FlexCell)

The first NexTech configuration analyzed in this study was a FlexCell. Dimensions of the various components of the FlexCell were obtained from NexTech along with two separate CAD files of the fuel manifold and honeycomb electrolyte. Significant efforts were required to integrate these CAD models with the anode and cathode layers to obtain a complete CAD model for the FlexCell. After the development of the CAD model, an incremental approach was adopted to perform numerical simulations by progressively adding more complexity. Initial simulations included the fuel manifold geometry without accounting for the electrochemistry. The aim of these simulations was to observe the flow

distribution among different channels. Because the honeycomb electrolyte of the FlexCell poses several numerical challenges, several simulations included a flat electrolyte and channels that were also shortened and reduced in number to lessen the number of grid elements, which are of the order of few millions. Finally, simulations were conducted that included honeycomb electrolyte. However, to reduce the number of elements the size of the geometry was reduced by one fourth and the plenum regions for both air and fuel manifolds were removed for simplification. One of the major challenges of this particular simulation was to generate a good quality grid, especially for the honeycomb regions. In our previous work, and most other numerical simulations reported by researchers, the anode-electrolyte interface shape has been planar. Thus, another challenging task was to handle the irregular shape of the interface between the anode and the electrolyte.

Figure 2(a) shows the flowfield geometry of the FlexCell. The manifold shapes are identical for both the fuel and air sides portions of the cell. Circular cross-sections shown in the figure indicate flow inlet and outlet ports. Because the initial simulations were conducted to analyze the flowfield in different channels of the manifold, electrochemistry/chemistry was not included. The velocity distribution on a plane passing through the fuel manifold is shown in Figure 2(b).

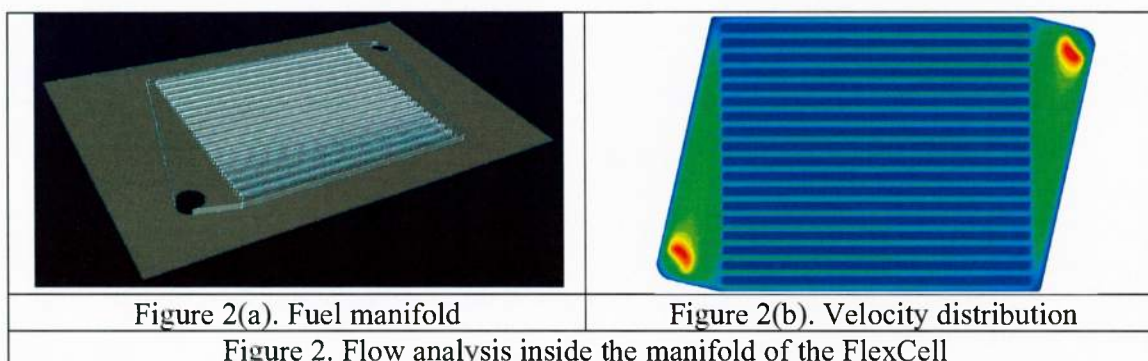
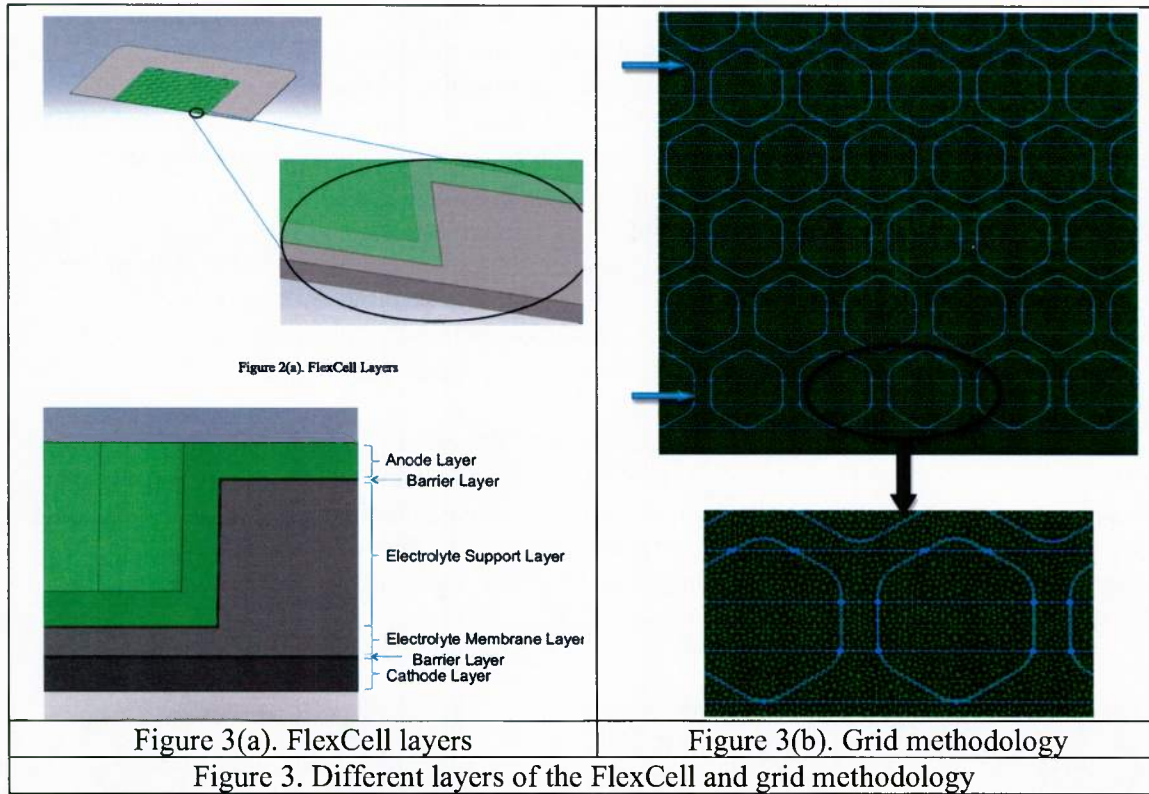


Figure 3(a) shows different layers of the FlexCell. As seen, the anode-electrolyte interface is not flat, which adds significant complexity in the numerical simulations. Also, generating grid for honeycomb regions is extremely difficult as shown in Figure 3(b). As seen, each hexagon is broken into several regions and sizes/shapes of various sub-regions are different for each hexagon.

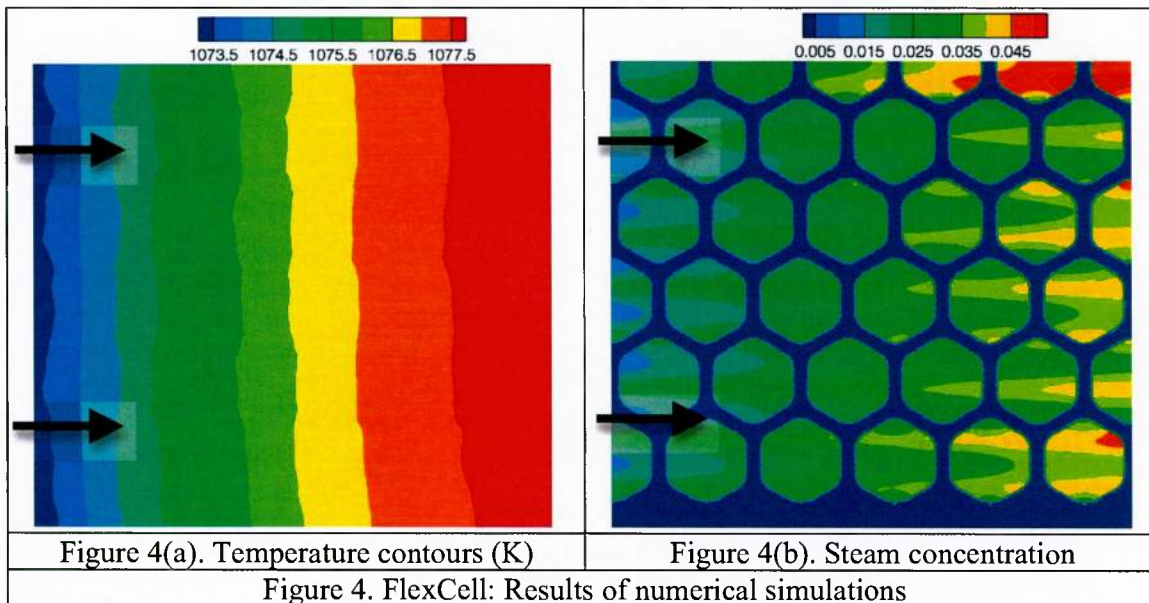


Figures 4(a) and 4(b) show results obtained on a truncated FlexCell with all relevant transport processes and electrochemistry included in the simulation. Mole fractions of different species included in this simulation along with operating conditions are described in Table 3. To control the number of grid elements, the geometry of the FlexCell has been reduced by one-fourth and the plenum regions for both fuel and air manifolds are removed.

Table 3. Mole fractions and thermodynamic conditions					
X_{H_2}	X_{H_2O}	X_{O_2}	X_{N_2}	$T(K)$	$P(N / m^2)$
0.95	0.05	0.21	0.79	1073 K	101325

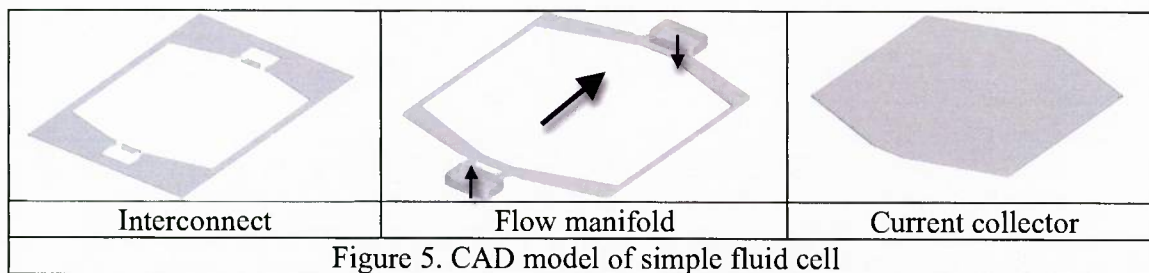
Figure 4(a) shows temperature contours in a plane passing through the honeycomb region. Because the electrochemical reaction associated with an SOFC is exothermic, a gradual increase in temperature is evident in the flow direction. The layer shown in the figure is made up of two different materials, namely anode and electrolyte. Both these materials have different thermal conductivities, which is responsible for the rough nature of the temperature contours shown in Figure 4(a).

Figure 4(b) shows steam concentration in a plane passing through the honeycomb region. Arrows in the figure indicate flow direction. Blue color in the figure indicates the electrolyte regions, which do not contain any chemical species. During the SOFC operation, steam is generated due to the electrochemical reaction. Thus, concentration of steam can be seen increasing in the figure. However, increase in steam concentration is not uniform in different hexagon regions. Various transport processes involved in SOFC operations and the location of each honeycomb with respect to the fuel channels are responsible for such behavior.



3.2 Case 2 (Simple Fluid Cell)

The reason behind specifying this cell as a “simple fluid cell” is that the analysis of this cell only includes fluid flow in different components of the cell. The primary purpose of this study was to compare numerical results obtained using the SimCenter code with the simulation results obtained by NexTech personnel. Different components of simple fluid cell are shown in Figure 5, which includes interconnect, flow manifold and current collector.



The current collector utilized in this model is made up of highly porous material (porosity = 0.9). As can be seen in Figure 5, fluid is entering vertically at the inlet port at 800°C and atmospheric pressure and flows through the current collector before leaving through the outlet port. The fluid containing the mixture of hydrogen and nitrogen with equal mole fractions is utilized in this simulation.

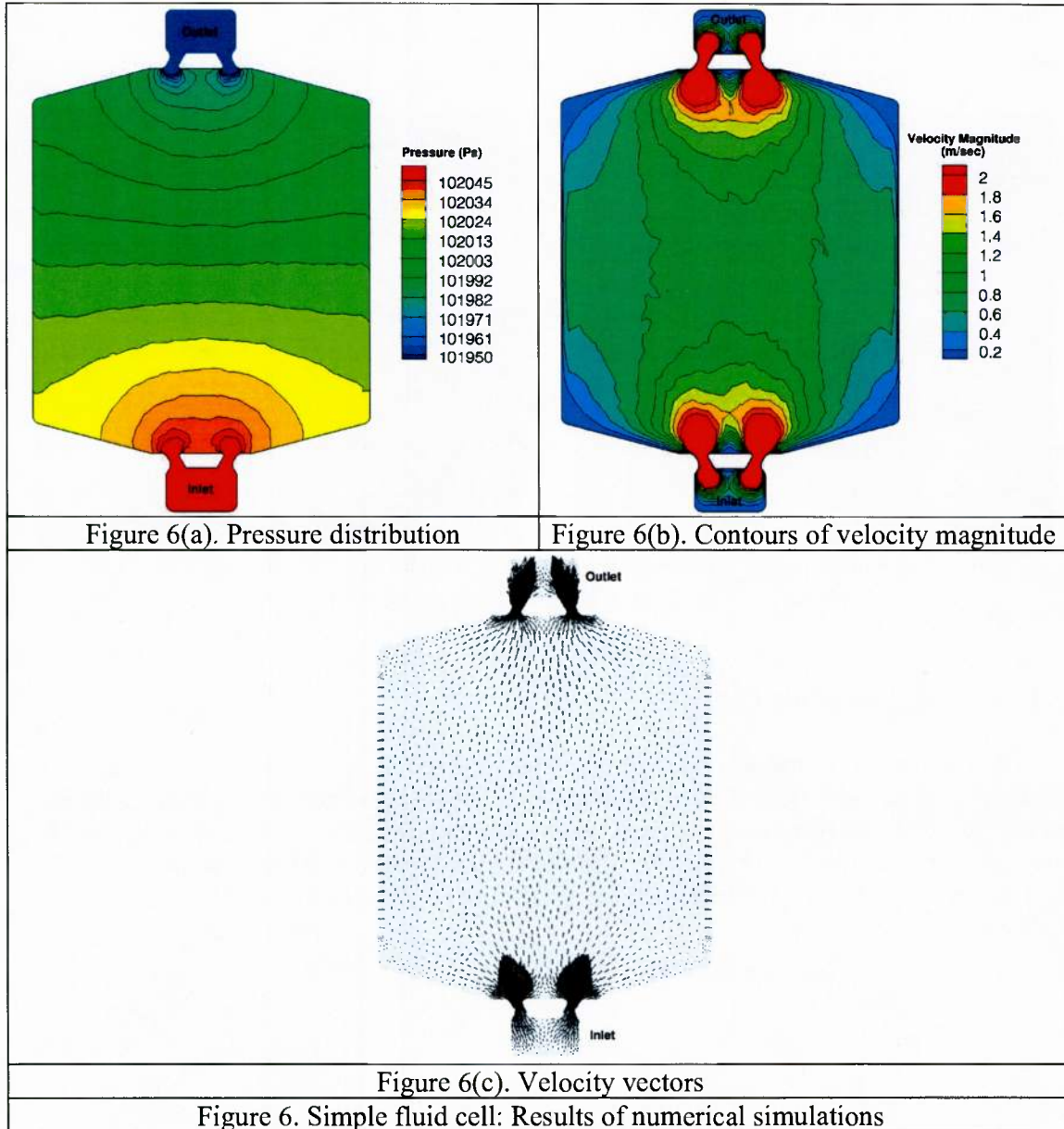


Figure 6(a) and (b) show pressure and velocity magnitude contours plotted on a plane extracted through the flowfield in streamwise direction. As expected, pressure is

reduced as fluid moves from the inlet towards the outlet port. NexTech personnel successfully compared the pressure contours plotted in figure 6(a) with their in-house numerical results both quantitatively and qualitatively. Figure 6(b) shows contours of velocity magnitude. The figure shows some interesting characteristics including, strong acceleration as flow enters from the inlet port to the main flowfield through two narrow passages and presence of regions with extremely low velocity magnitude located at four corners of the flowfield. Results shown in Figure 6(b) also compared favorably with the NexTech results. To further demonstrate the flow patterns, velocity vectors are plotted on a streamwise plane in Figure 6(c). As seen, vectors show uniform pattern throughout the domain except in the corners.

3.3 Case 3 (28 mm cell)

The third CAD model received from NexTech is shown in Figure 7. The computational model contains all SOFC components including flow channels, electrodes, electrolyte, interconnects, current collectors and seals. Figure 8(a) and 8(b) show shapes of anode and cathode current collectors, respectively. As seen, geometry of this cell is quite complicated mainly due to the shape of the current collectors and the manner in which current collectors are connected with other components of the cell. While model was still in the meshing phase, the decision to move to the more important G13 cell was made during discussion with NexTech. Even though analysis was not performed on this cell, significant efforts were made to generate mesh for this complicated computational model.

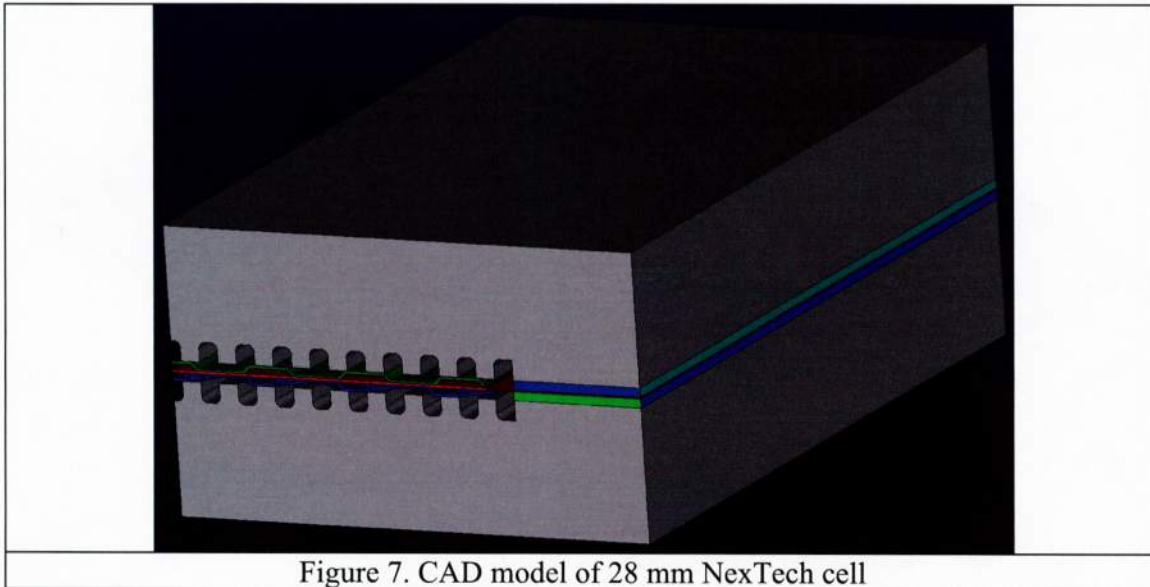
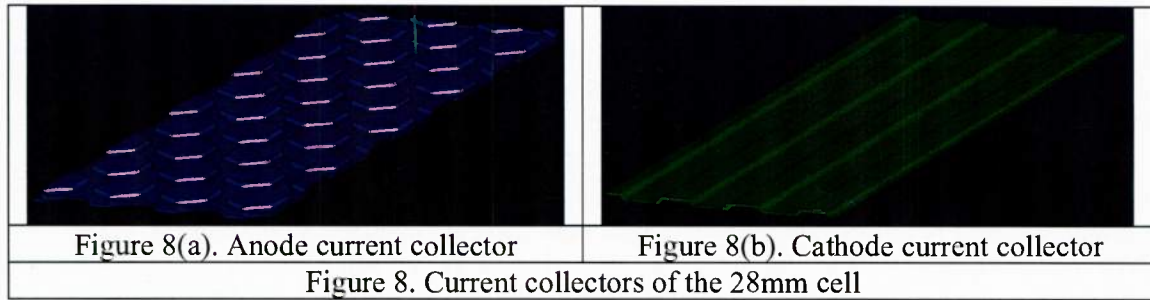
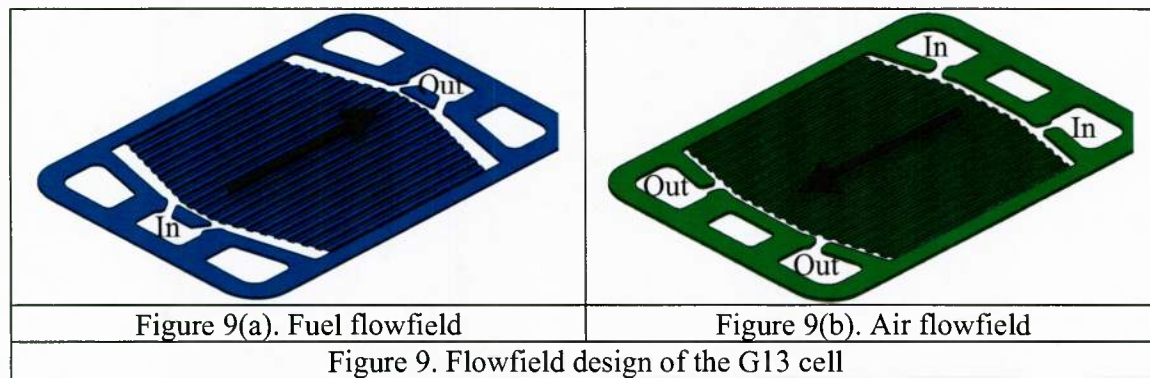


Figure 7. CAD model of 28 mm NexTech cell



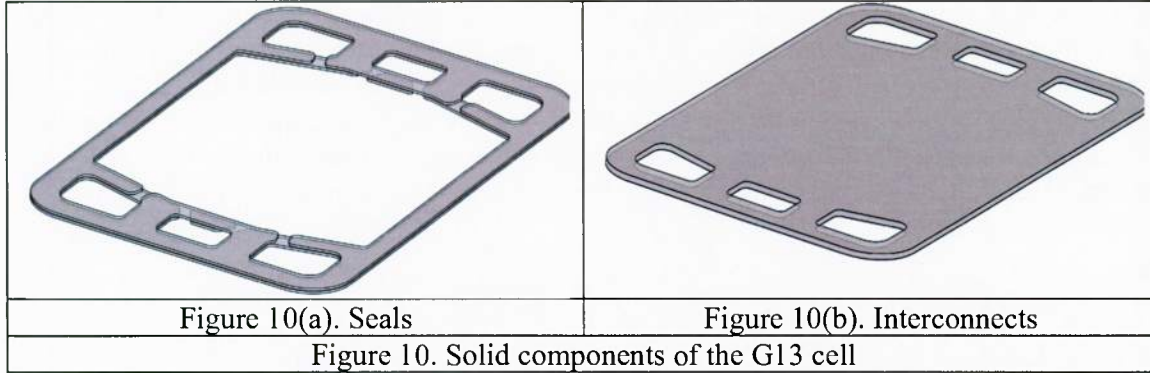
3.4 Case 4 (G13 cell)

As mentioned earlier, analysis of G13 cell was prioritized over 28 mm cell after discussion with NexTech personnel. Different components of G13 cell are shown in Figures 9 and 10. Fuel flowfield, made up of fuel manifold and anode current collector is shown in Figure 9(a). The design of the fuel flowfield is inspired by the simple fluid cell described in Case 2. Figure 9(b) shows air flowfield comprising of air manifold and cathode current collector. In the initial CAD model received from NexTech, shapes of the anode and cathode currents collectors were not exactly the same. However, it was later decided to use the same shape (as the anode current collector) for both current collectors to simplify the model. Electrodes and electrolyte are sandwiched between the flowfields shown in Figure 9. To avoid mixing of fuel and air, seals are utilized on both sides (Figure 10(a)). All these components are enclosed on top and bottom by the interconnects shown in Figure 10(b).



The inlet and outlet ports for both air and fuel manifolds are indicated in Figure 9. As air and fuel flow in the opposite directions, the flow arrangement is counter-flow. Fuel mixture and air enter through appropriate inlet ports and diffuse inside current collectors and electrodes. Oxygen atoms combine with the electrons inside an extremely thin layer near the cathode-electrolyte interface and are converted into oxygen ions ($0.5O_2 + 2e^- \rightarrow O^{2-}$). These oxygen ions migrate through the solid electrolyte to reach the anode-electrolyte interface and combine with hydrogen to generate steam and release

electrons ($H_2 + O^{2-} \rightarrow H_2O + 2e^-$). Both these reactions take place inside extremely thin layers near the cathode-electrolyte and the anode-electrolyte interfaces, respectively. Because modeling the details of the interface region is impractical due to the small size, the cumulative effect of the electrochemical reactions is modeled as a jump in the electric potential, which is determined using Nernst potential (equation (18)) and activation polarization (equation (17)).



The fuel mixture is assumed to contain hydrogen and steam only, i.e. chemistry is not present in this case. Air is modeled as a mixture of oxygen and nitrogen. Species mole fractions of the fuel mixture and air entering the flowfields are given in Table 4 along with the operating pressure and temperature of both fuel and air.

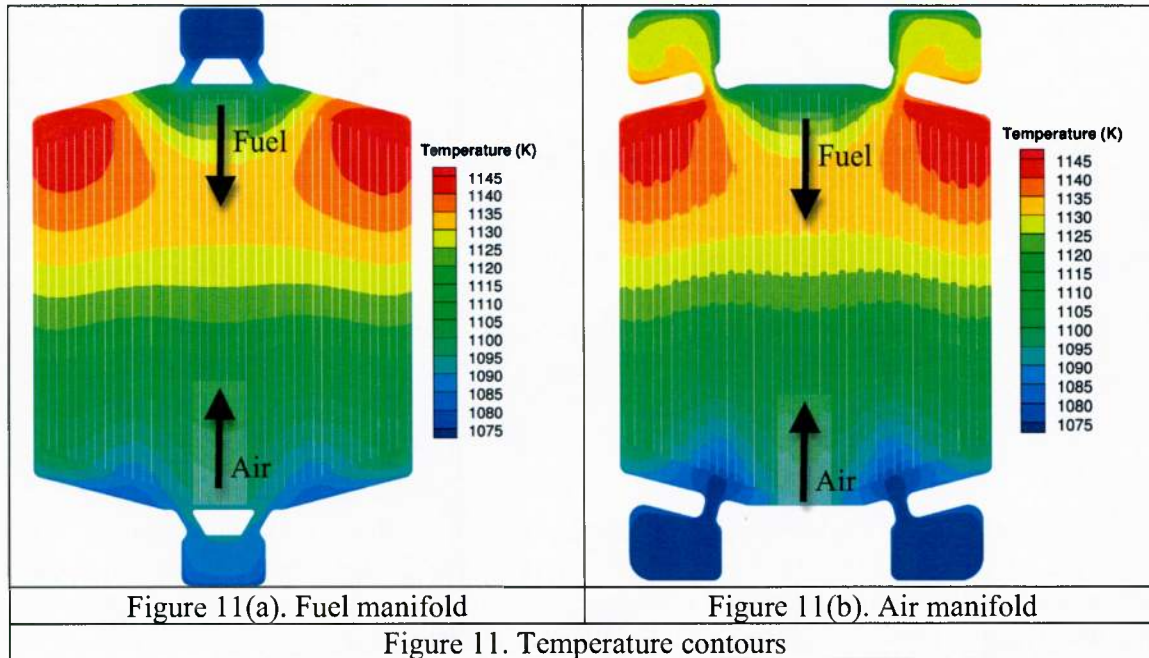
Table 4. Mole fractions and thermodynamic conditions					
X_{H_2}	X_{H_2O}	X_{O_2}	X_{N_2}	$T(K)$	$P(N / m^2)$
0.95	0.05	0.21	0.79	1073 K	101325

Figures 11- 13 show temperature contours plotted on planes extracted through different components of the G13 cell in streamwise direction. Temperature is continuous in the entire domain unlike potential or concentration fields. As mentioned earlier, various modes of energy transfer includes convection/diffusion/conduction of energy, heat generated due to viscous stresses and most importantly, heat generated due to entropy changes occurring because of the electrochemical reaction at the anode-electrolyte interface. Also, Ohmic heating contributes to the rise in temperature.

The extent of temperature rise depends strongly on the mass flow rates of fuel and air. Convective cooling increases with higher flow rates of either fuel or air and thus, contributes towards reduction in average temperature rise. The opposite is true for the lower mass flow rates. Current density is another major contributor in temperature rise as Ohmic heating is linearly proportional to the current density. Also, current density dictates

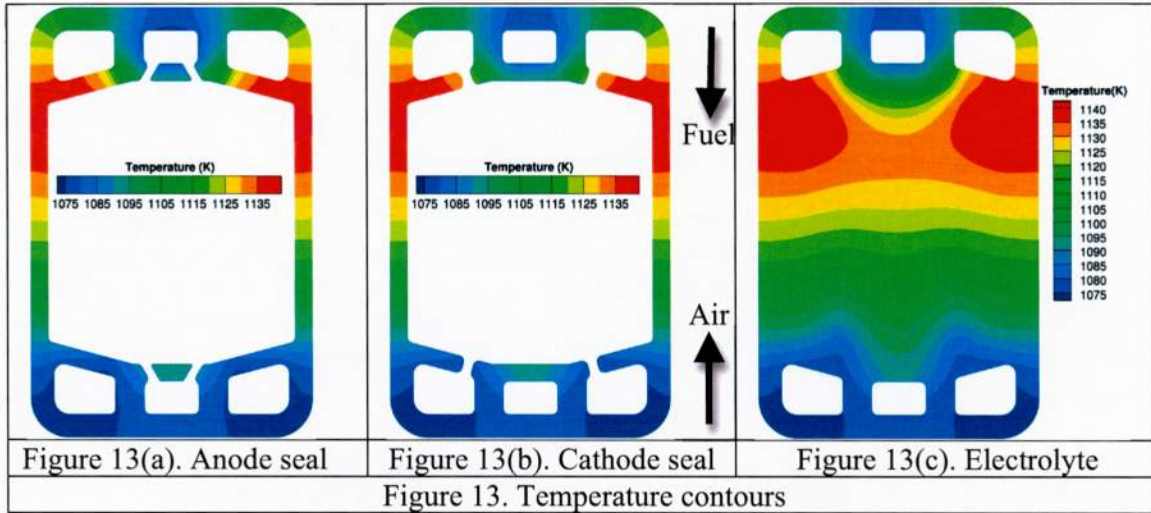
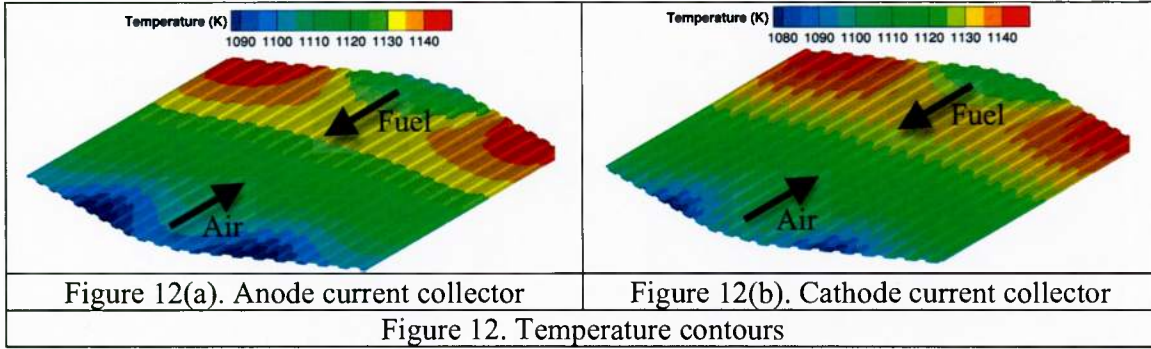
the extent of electrochemical activity at the electrode-electrolyte interface that is responsible for generating heat.

Figures 11(a) and (b) show temperature contours plotted on planes passing through fuel and air manifolds, respectively. Flow directions of both fuel and air are also indicated. In figure 11(a), fuel enters the inlet port at 1073 K and there is a gradual rise in fuel temperature due to the heat generated by electrochemical reaction. As fuel moves through the flowfield, temperature starts reducing due to the cooling effect of the incoming air from the opposite direction. The reduction in fuel temperature continues until it leaves through the outlet port. In figure 11(b), air enters through the inlet port at 1073 K and gradually heats up as it passes through the flowfield. The rise in the temperature of air is continuous throughout the domain unlike fuel until it reaches the outlet port, when it begins to cool down. Overall, temperature of fuel is lower than the temperature of air leaving from the respective outlets.

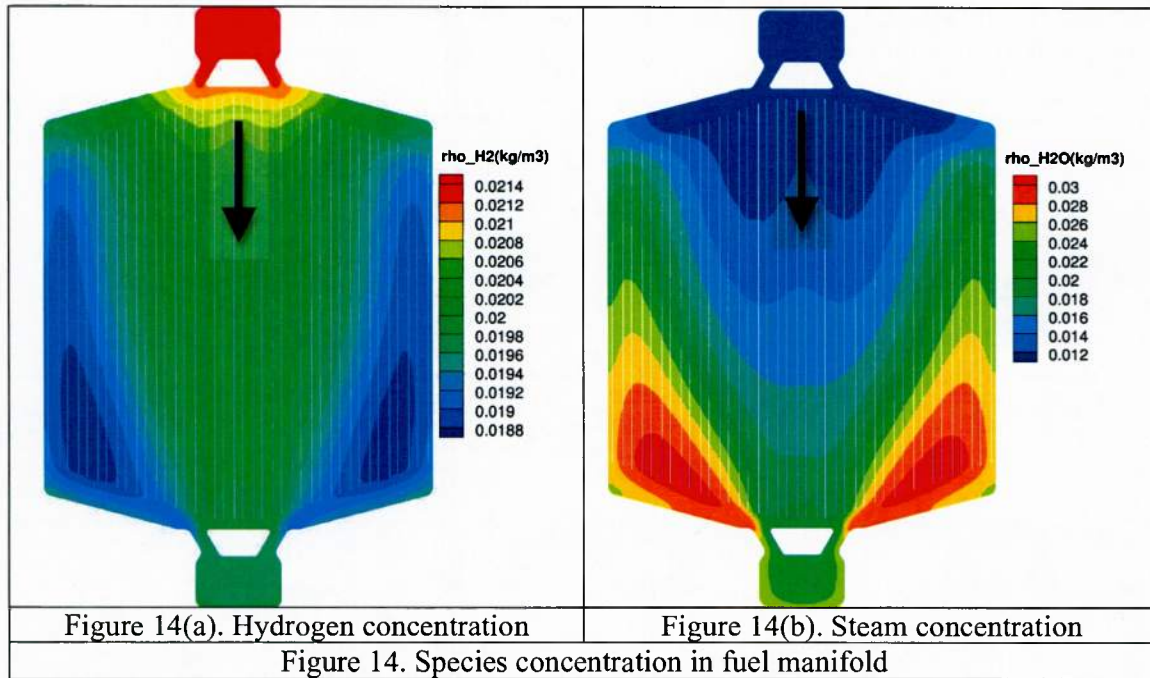


Figures 12(a) and (b) show temperature contours plotted on planes passing through the anode and cathode current collectors, respectively. A lot of similarities can be found between the characteristics of these contours and the contours shown in figure 11(a) and (b) including spots indicating higher and lower temperature regions. Figures 13(a), (b) and (c) show temperature contours plotted on planes passing through the anode seal, cathode seal and electrolyte, respectively. Again, temperature distribution inside these components exhibits similarities with those shown in Figures 11 and 12. Similarities in temperature contours inside different components of the cell indicate that the temperature gradient

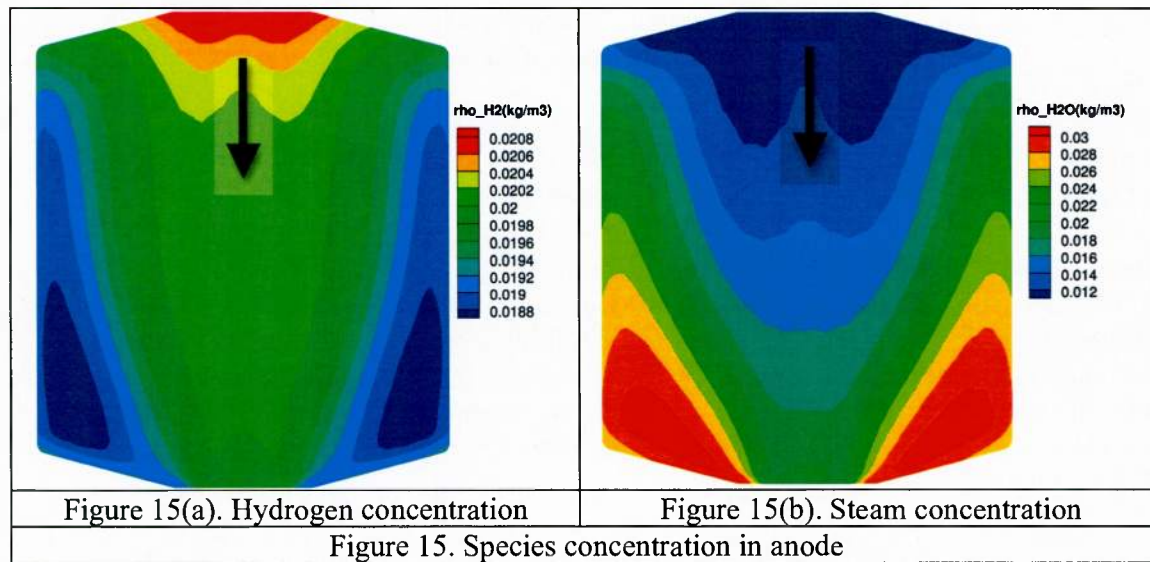
through the thickness of the cell is negligible due to the small thickness of the cell compared to other dimensions.

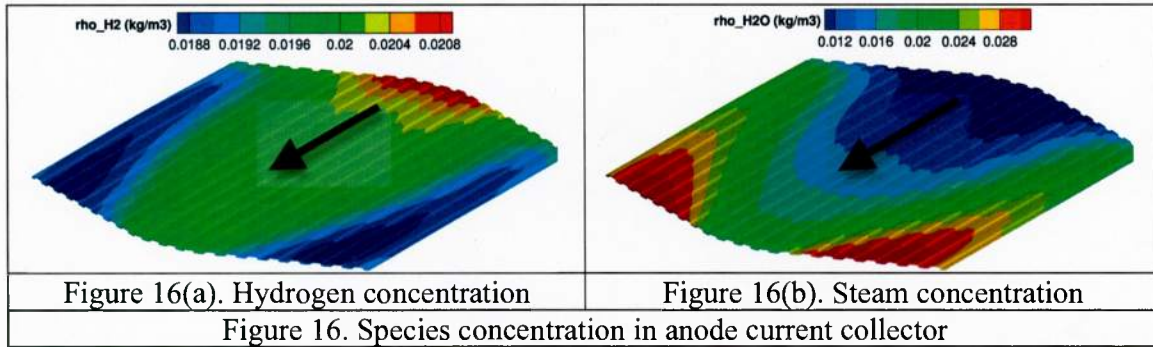


Figures 14(a) and (b) show hydrogen and steam contours plotted on a plane passing through the fuel manifold in streamwise direction. Figure also indicates the flow direction of the fuel. In electrochemical reaction, hydrogen acts as a reactant while steam is a product. Thus, hydrogen concentration reduces as fuel flows from the inlet port towards the outlet port. Non-uniformity in reduction of hydrogen concentration is evident in Figure 14(a), especially left and right sides of the domain show the lowest concentration. One of the reasons behind this behavior is that the fuel flow rate in the affected area is low compared to the rest of the domain. Further discussion regarding flow rate is presented in the later part of this report. On the other hand, steam concentration, which is a product of the electrochemical reaction, increases as fuel flows through the domain as shown in Figure 14(b).

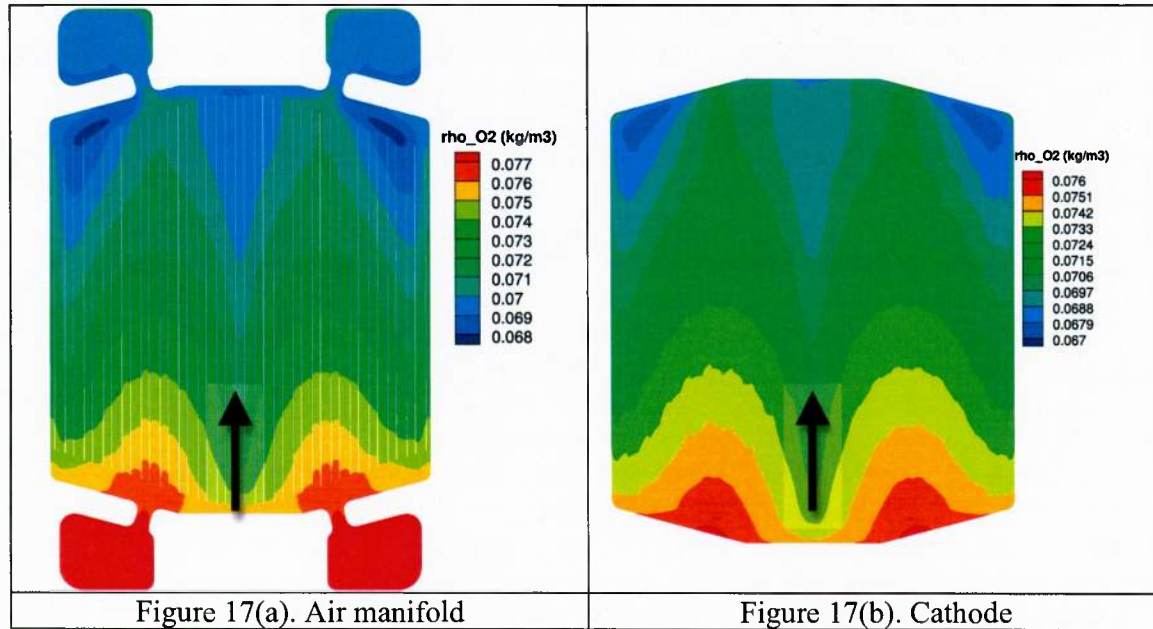


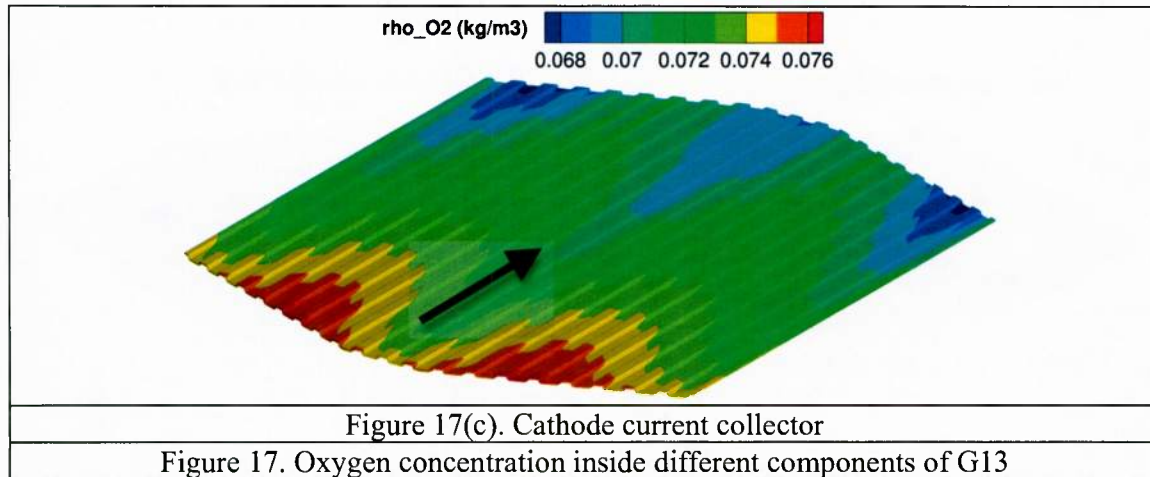
Figures 15 and 16 show contours of hydrogen and steam concentration on planes extracted in streamwise direction through anode and anode current collector, respectively. Characteristics of concentration contours in figure 15 and 16 are similar to those discussed for figure 14 in previous paragraph. This suggests strong species diffusion through the thickness of the cell. One of the reasons for such behavior is small thickness of different components of the cell.





Figures 17(a), (b) and (c) show contours of oxygen concentration on planes extracted through air manifold, cathode and cathode current collector, respectively. As oxygen is a reactant of the electrochemical reaction, its concentration reduces as air flows through the cell. As shown for the hydrogen and steam, oxygen contours plotted through different components in figure 17 exhibit similar characteristics indicating strong species diffusion through the thickness of the cell. Spots with the lowest oxygen concentration (top-left and top-right corners) have strong relationship with the air flow rate. Further discussion on this topic is covered in the later part of this report.





Figures 18(a) and (b) show contours of streamwise velocity (z-direction) plotted on planes passing through fuel and air manifolds, respectively. These are some interesting features present in both plots. Non-uniformity in fuel flow rate is evident in figure 18(a) as majority of fuel is passing through the middle region of the manifold. The reasons behind such behavior include the placement of the inlet port with respect to the main flowfield and the angles of the narrow passage through which fuel enters the flowfield. The starving areas are located at four corners of the flowfield in figure 18(a). Unlike fuel manifold that has one inlet and exit port, air manifold contains two inlet and exit ports. Thus, flow distribution inside air manifold is completely different that that of the fuel manifold. Due to the placement of the inlet ports and angle at which air enters the main flowfield, areas with high flow rate are located between the center and the sides of the domain in figure 18(b). Again, the starving regions are located at the corners in figure 18(b). For both air and fuel manifolds, corners represent the most affected regions due to low flow rates of respective fluids, which may adversely affect the cell efficiency and lead to localized heating.

Figures 19-23 show stress distribution inside different components of the G13 cell. All components are considered stress free at 800°C. The stress contours are generated by the in-house structures code using flowfield data (temperature) imported from the fuel cell code. SOFC is manufactured by connecting various components that possess different material properties. Thus, mismatch in coefficients of thermal expansion of these components contribute greatly towards stress generation in SOFC. Figures 19(a) and (b) show contours of mean principal stress (MPS) plotted on outer surface of the anode and cathode current collectors, respectively. As seen, stress distribution in both current collectors is uniform except at some outer edges, where current collectors are connected with other cell components.

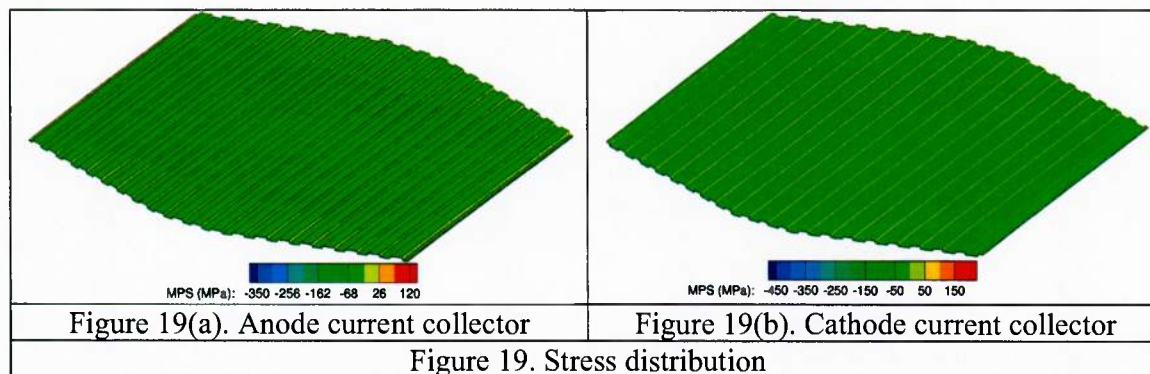
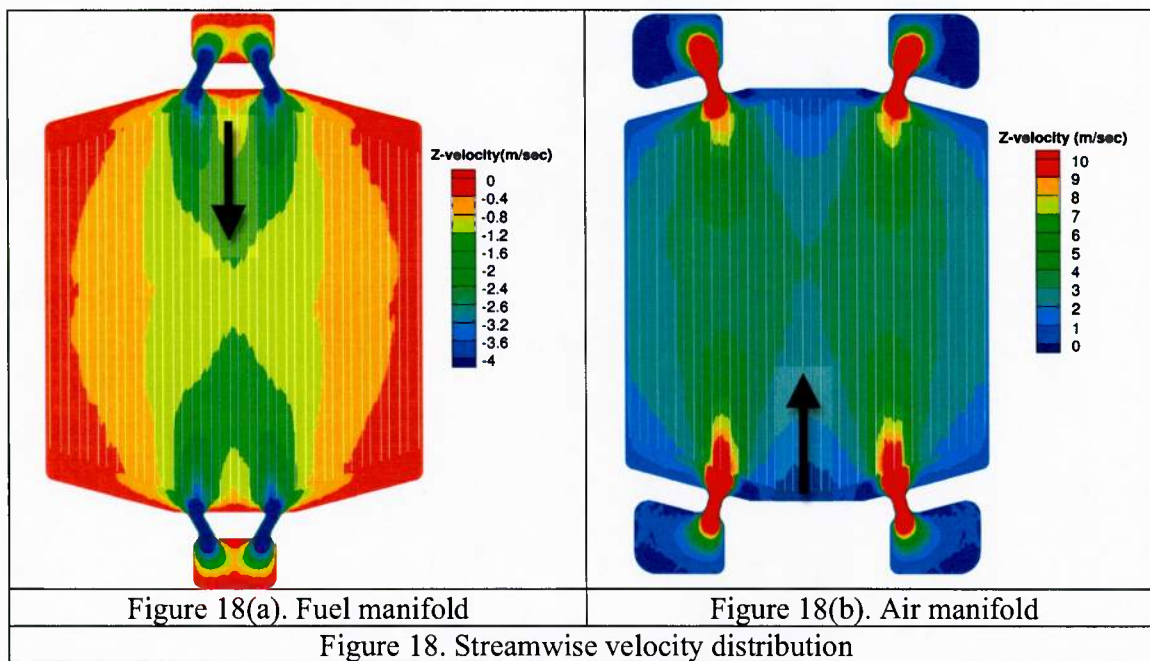
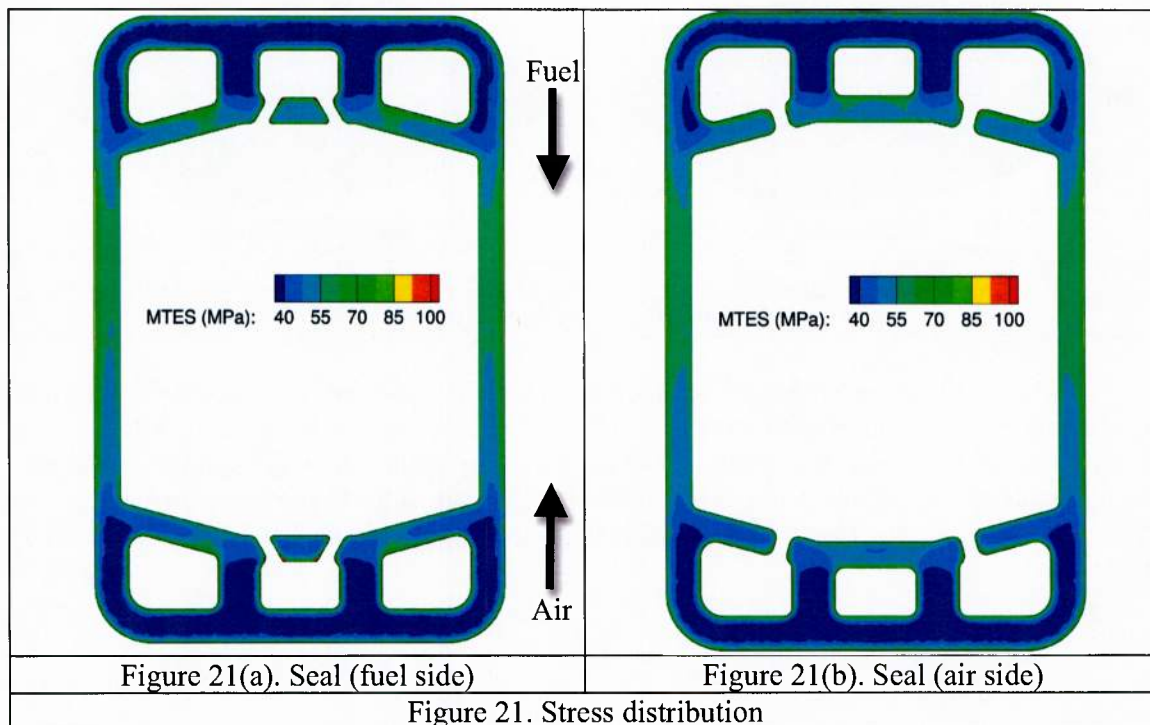
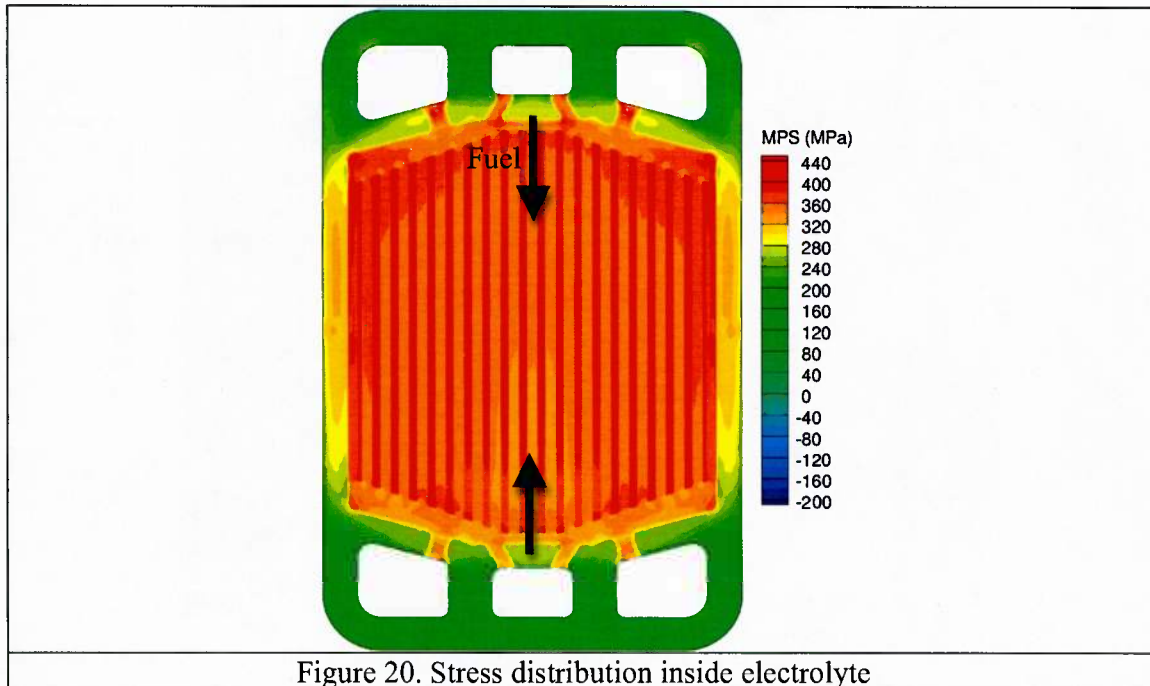
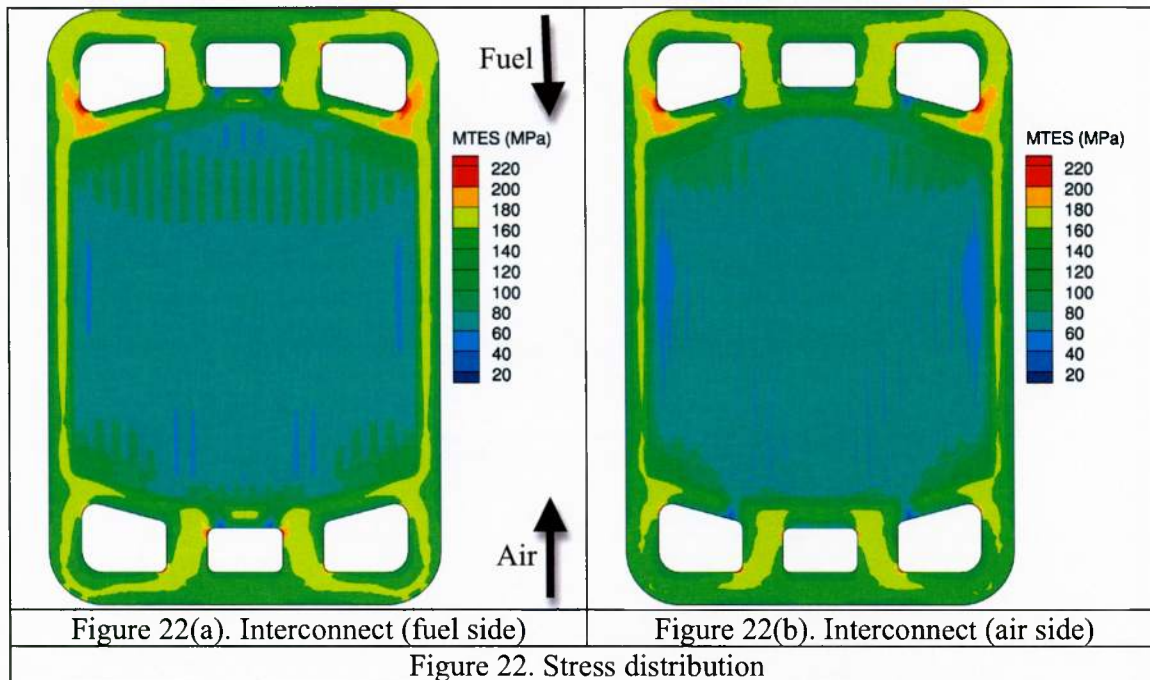


Figure 20 shows MPS contours plotted on a plane extracted through the electrolyte in streamwise direction. Higher values of MPS are present near the active area, where electrochemical reaction takes place. Also, electrolyte is connected with anode and cathode on each side of this region. Thus, mismatch in coefficients of thermal expansion and presence of exothermic electrochemical reactions are responsible factors for high stress in this region.



Figures 21(a) and (b) show maximum tresca equivalent stress (MTES) plotted on planes passing through seals located on fuel and air sides, respectively. Overall, stress distribution is uniform in both figures. A close observation indicates isolated spots with high stress values located on the edges surrounding inlet and outlet ports of both fuel and air manifolds.

Figures 22(a) and (b) show MTES contours plotted on planes passing through the interconnects located at the bottom (fuel side) and top (air side) of the cell, respectively. As clearly seen, regions with maximum stress are located near air outlet ports in both figures. Also, tiny spots with high stress values are present near fuel inlet port in both figures. Characteristics of stress contours in Figure 22 are similar to those for the seals shown in Figure 21.



3.5 Case 5 (Simplified SOFC)

The fluid-structure interaction capability demonstrated in the previous case was initially developed for the simplified SOFC described in this case. The development was performed while waiting for the arrival of new cluster and storage system to be used to run simulations on NexTech's G13 cell. The geometry of the cell utilized in this case is shown in Figure 23. As seen, computational model includes all relevant SOFC components including fuel/air manifolds, electrodes/electrolyte (PEN), seals and interconnects. The number of channels for both air and fuel manifolds is chosen to be twelve to make the geometry mimic realistic planar SOFC. Various geometric dimensions of the cell are listed in Table 5.

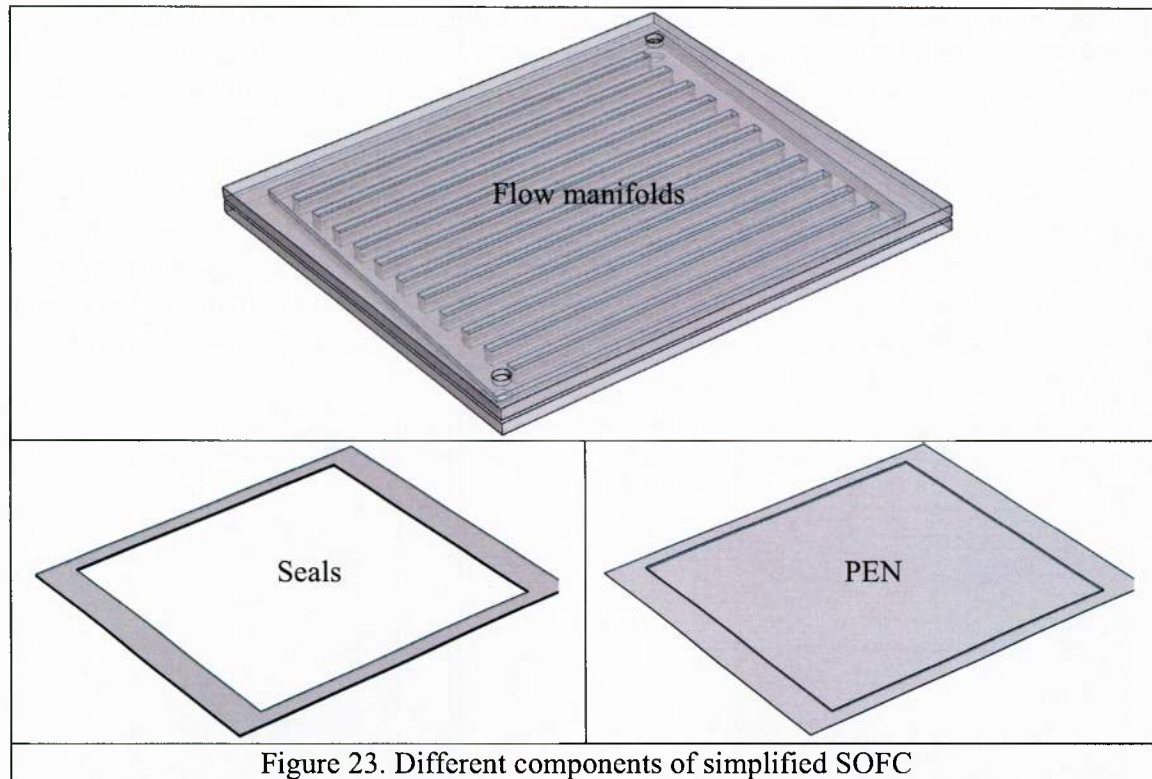


Figure 23. Different components of simplified SOFC

Table 5. Geometrical dimensions of simplified SOFC	
Length	43.0 mm
Width	39.0 mm
Height	0.23 mm
Anode thickness	0.1 mm
Cathode thickness	0.1 mm
Seal thickness	0.1 mm
Electrolyte thickness	0.1 mm
Interconnect thickness	0.5 mm
Channel thickness	0.5 mm

No-slip, adiabatic wall boundary conditions are applied at the top wall, bottom wall and side walls of the computational geometry shown in Figure 23. As mentioned previously, fixed potential ($\phi = 0$) boundary condition is applied at the bottom wall, while

the top wall is treated by specifying average current density ($i = i_{\text{applied}}$). Inflow boundary conditions with specified mass flow rate and species mole fractions are applied at both fuel and air channel inlets. The temperature of the air and fuel mixture entering from their respective inlet ports is 1073 K. Also, both fluids are operating at atmospheric pressure. Specified back pressure outflow conditions are applied at both air and fuel outlet ports. Initial species mole fractions and thermodynamic conditions utilized in this simulation are given in Table 6. As seen in Table 6, partially reformed fuel has been utilized and thus, methane reforming and water gas shift reactions have been considered inside the anode. Current density of 5500 Am^{-2} is applied at the top wall of the computational geometry shown in Figure 23.

Table 6. Mole fractions and thermodynamic conditions

X_{CO}	X_{H_2O}	X_{CO_2}	X_{H_2}	X_{CH_4}	X_{O_2}	X_{N_2}	$T(K)$	$P(N \text{ m}^{-2})$
0.029	0.493	0.044	0.263	0.171	0.198	0.802	1073 K	101325

Two different configurations co-flow and counter-flow, are analyzed in this case. Figures 24(a) and (b) show temperature contours plotted over outer surface of the cell for co-flow and counter-flow configurations, respectively. Figures also show flow directions of both air and fuel. As expected, in co-flow case, there is a gradual rise in temperature as both fuel and air move through the flow domain. Heat generated due to the electrochemical reaction is the main factor affecting the increase in temperature. In counter-flow case, regions showing maximum temperature are present in the middle of the computational domain. Also, maximum temperature found in the co-flow case is higher than the same found in the counter-flow case.

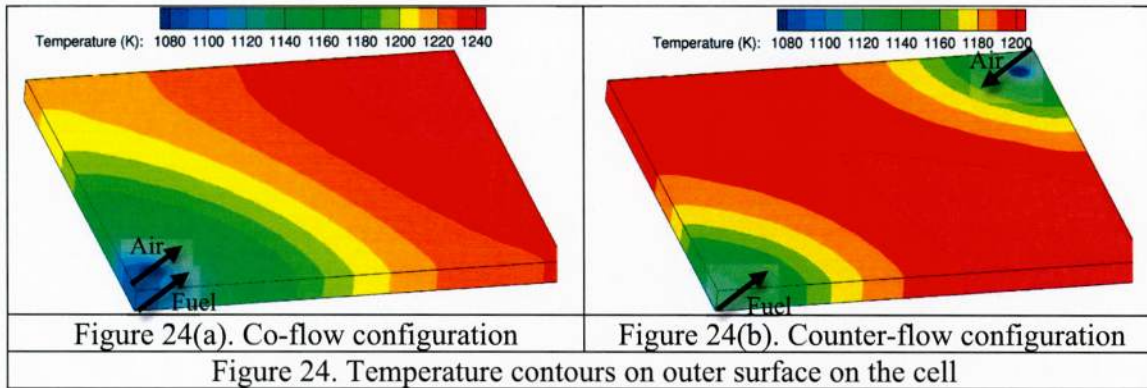
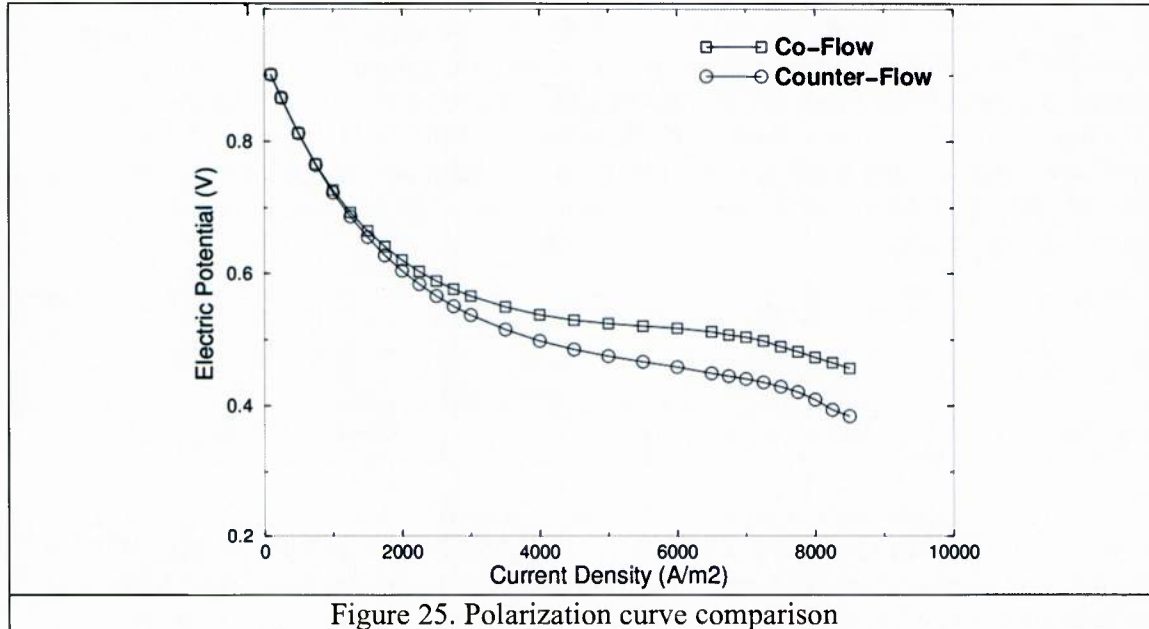
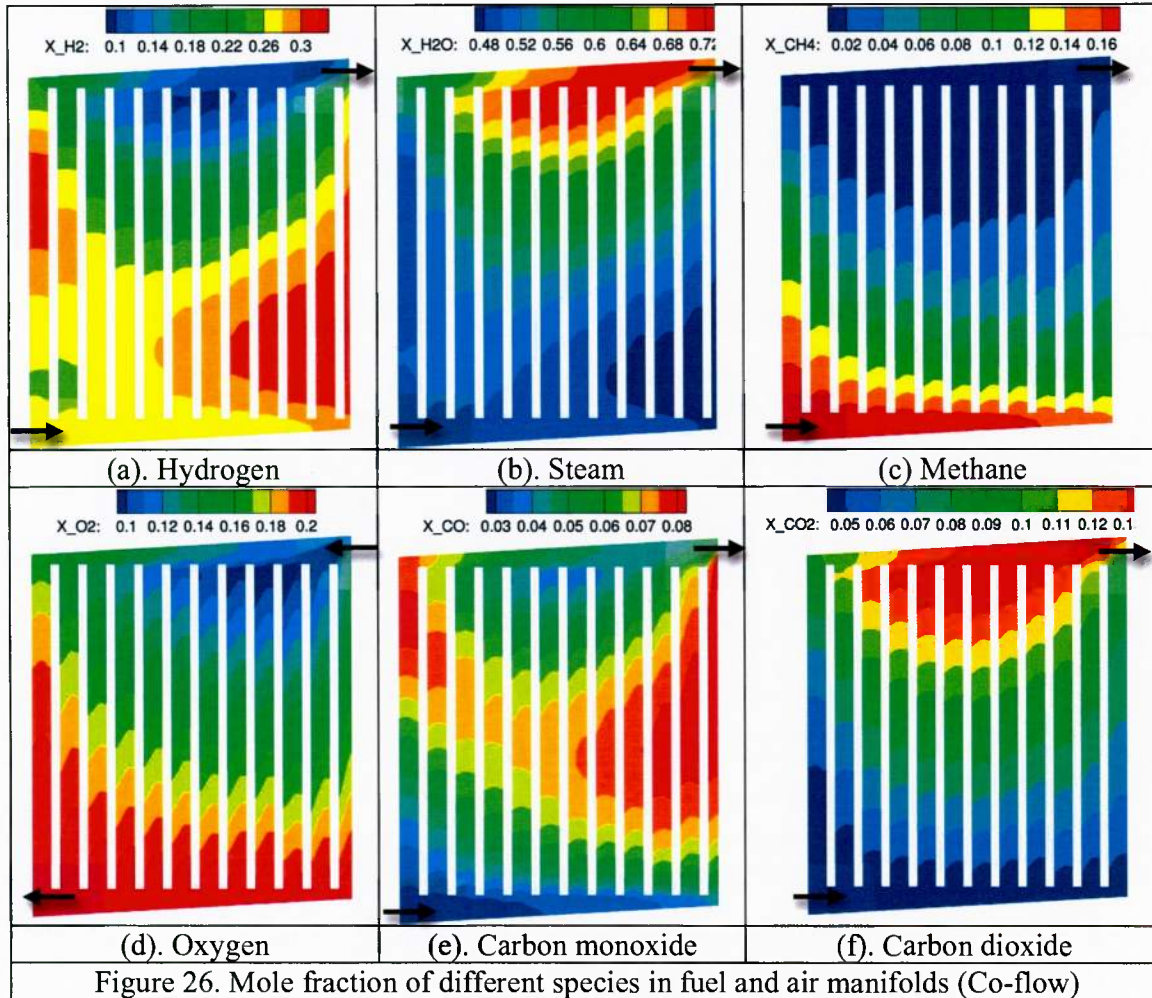


Figure 25 shows polarization curves plotted for both co-flow and counter-flow cases operating under the same conditions described in Table 6. As expected, cell voltage reduces with increase in current density due to the effects of several irreversibilities present inside the cell. Both cases exhibit similar performance for low current densities. However,

as current density increases, co-flow configuration performs better than the counter-flow configuration.



Figures 26 (a) – (f) show mole fractions of different species plotted on planes passing through fuel and air manifolds for the co-flow case. As mentioned earlier, two chemical reactions namely, methane reforming and water-gas shift reactions are considered inside the anode electrode. Also, electrochemical reaction, which is responsible for the production of steam and consumption of hydrogen and oxygen, affects species distribution in the flowfield. In figure 26(a), there is an overall reduction in hydrogen concentration as it moves through the flowfield. A region located near bottom right corner of the plane shows rise in hydrogen mole fraction. This behavior is caused by hydrogen production due to methane reforming reaction. In figure 26(b), gradual rise in steam concentration due to electrochemical reaction is evident as fuel moves from the inlet to the outlet of the manifold. Methane mole fraction is plotted in figure 26(c). As methane reforming is a fast reaction, most of the methane can be seen consumed in the first half of the flowfield. Figure 26(d) shows oxygen mole fraction plotted on a plane extracted from the air manifold. As oxygen is a reactant of the electrochemical reaction, there is gradual reduction in its mole fraction as air moves through the flowfield. Contours of carbon monoxide (CO) mole fraction plotted in figure 26(e) exhibit non-uniformity in the flowfield. As CO acts as a reactant in shift reaction and as a product in reforming reaction, their combined effect produces non-uniformity in the contours shown in figure 26(e). Finally, contours of carbon dioxide mole fraction are plotted in figure 26(f). As the only reaction involving carbon dioxide (as a product) is a shift reaction, gradual rise in carbon dioxide concentration is evident in figure 26(f).



Figures 27(a) – (f) show stress contours plotted on planes extracted through different solid and porous components of the cell for co-flow configuration. Figures 27(a) and (b) show contours of MTES plotted on streamwise planes passing through seals located on both fuel and air sides, respectively. As seen, maximum stress is present near fuel inlet port in both figures. Figure 27(c) – (e) show contours of MPS plotted on planes passing through the anode, electrolyte and cathode, respectively. Some characteristics of these contours such as location of the maximum stress region are similar in all three plots. This region is located near fuel inlet port in the computational domain. Figure 27(f) shows contours of MTES plotted on a vertical plane passing through the interconnect and inlet ports. As expected, maximum stress is found near fuel inlet port. Regions near air inlet port also indicate high values of MTES. Overall, maximum stress values are found in a plane extracted through the anode electrode in figure 27(c).

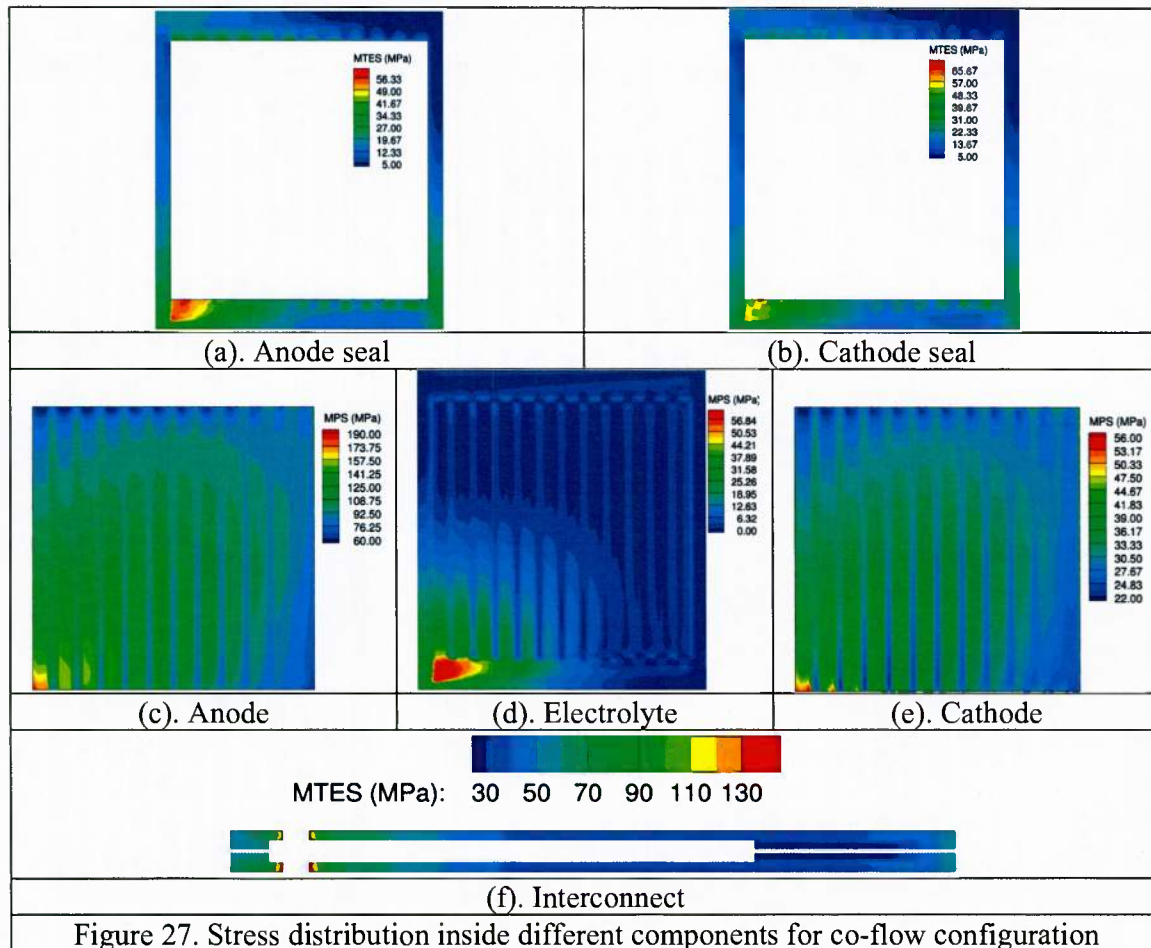


Figure 27. Stress distribution inside different components for co-flow configuration

Figures 28(a) – (f) show stress contours plotted on planes extracted through different components of the cell for counter-flow configuration. Even though air is flowing in the opposite direction in this case compared to the previous case (figure 27), stress contours in different components show similar characteristics in both cases. Regions with maximum stress are located near fuel inlet port in different cell components. Overall, stress values for the counter-flow case are smaller than the co-flow case.

As mentioned earlier, both fuel cell and structures code are capable of performing sensitivity analysis. To demonstrate this capability, stress sensitivity contours are plotted on planes extracted through different components of the cell in figures 29(a) – (e). The co-flow configuration is utilized in figure 29. Design variable in this study is cathode porosity. The method utilized to compute sensitivity derivatives is direct differentiation in both fuel cell and structures code. Structures code requires values of flowfield variables and sensitivities of flowfield variables from the fuel cell code to compute stress sensitivities. The characteristics of stress sensitivity contours in figure 29 are similar to those shown for

the stress contours in figure 27; especially regions with highest sensitivity values are located near fuel inlet port for all components.

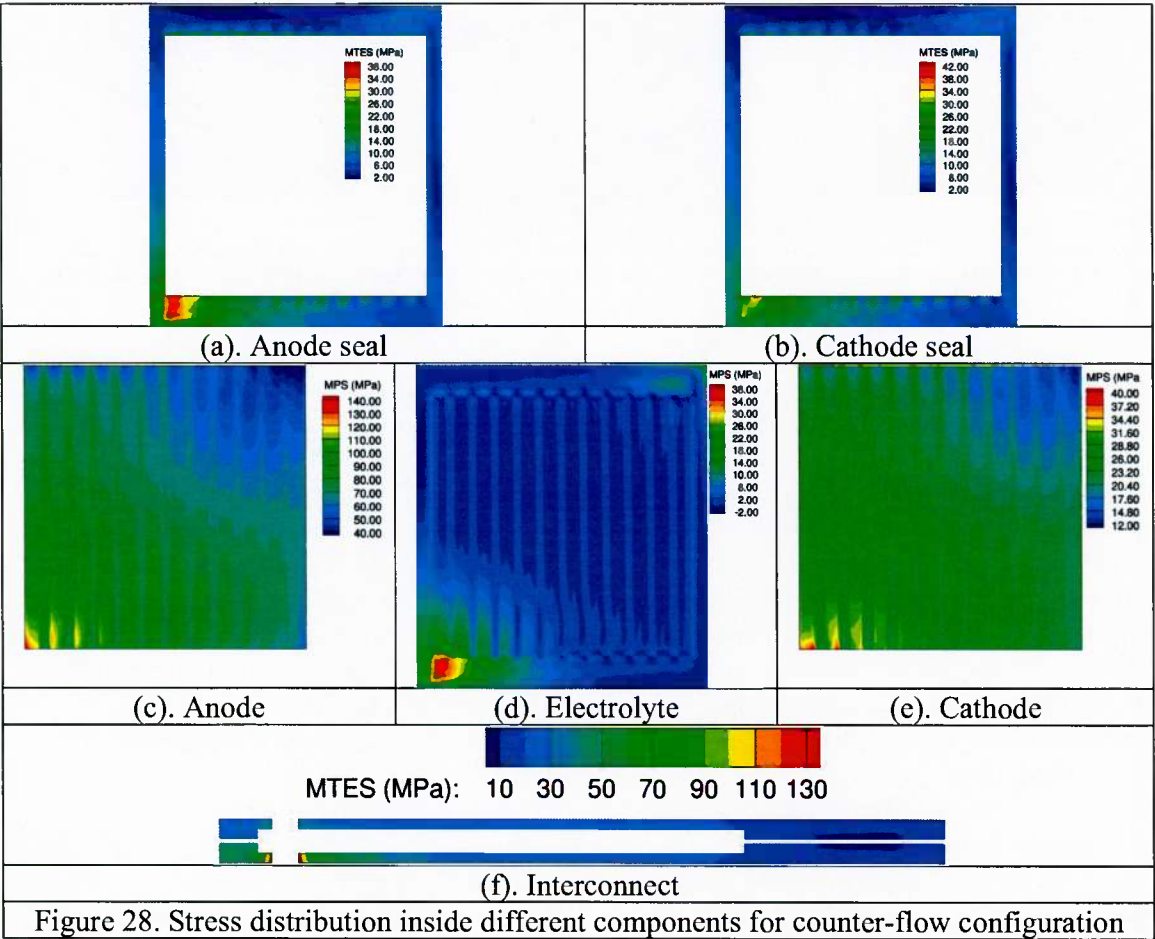
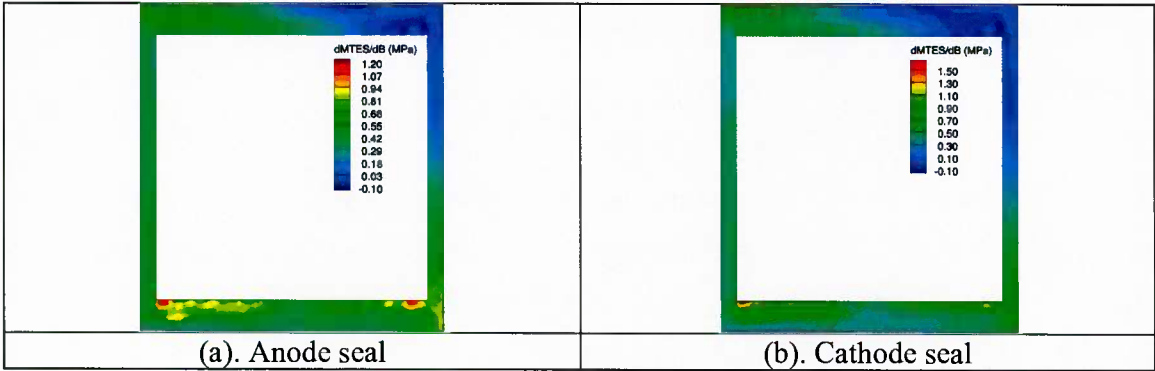
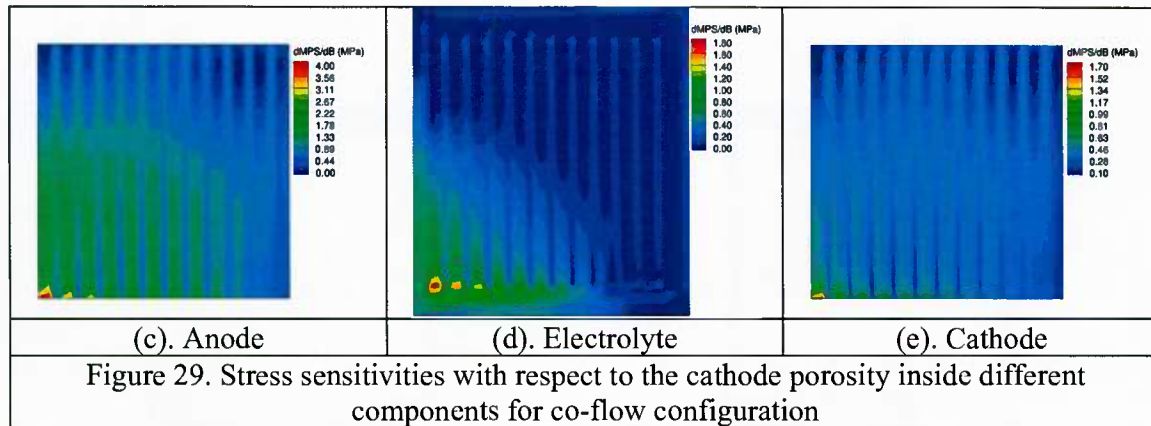


Figure 28. Stress distibution inside different components for counter-flow configuration





4. Conclusions

A three-dimensional, parallel, unstructured solver has been developed to model complicated transport phenomena present inside all components (channels, electrodes, electrolyte, seals, current collectors and interconnects) of different cell configurations provided by NexTech Materials. A capability to perform thermo-mechanical analysis of different components of SOFCs has been developed by coupling the fuel cell code with the structures code. Results obtained using this capability indicate that the main factors affecting the stress distribution are temperature gradients and mismatch of coefficients of thermal expansion between different components of the cell. Also, capability to perform thermo-mechanical sensitivity analysis has been developed using direct differentiation method. Using this capability, sensitivity derivatives of stress has been computed for a simplified SOFC geometry.

Acknowledgements

This work was supported by the Office of Naval Research grant number N000141010462, Planar Solid-Oxide Fuel Cell Research and Development. This support is greatly appreciated.

Nomenclature

Symbols	Name	Unit
B	Permeability	m^2
E_t	Total energy	J m^{-3}
f	Cost function	cost function depended
H	Enthalpy	J kg^{-1}
i	Current density	A m^{-2}
i_0	Exchange current density	A m^{-2}

J	Mass flux vector	$\text{kg m}^{-2} \text{s}^{-1}$
\dot{m}	Mass flow rate	kg s^{-1}
M	Molecular weight	kg kmol^{-1}
ns	Number of species	-
P	Pressure	N m^{-2}
Q	Solution vector	solution variable dependent
q	Heat flux	$\text{J m}^{-2} \text{s}^{-1}$
T	Temperature	K
u	x-velocity component	m s^{-1}
v	y-velocity component	m s^{-1}
w	z-velocity component	m s^{-1}
X_i	Mole fraction of i^{th} species	-

Greek Symbols

β	Design variable vector	design variable dependent
χ	Grid vector	m
ρ	Mass concentration	kg m^{-3}
μ	Molecular viscosity	kg m s^{-1}
ϕ	Electric potential	volt
η	Activation polarization	volt
ε	Porosity	-
κ	Tortuosity	-
V	Control volume	m^3
τ	Viscous flux	$\text{kg m}^{-1} \text{s}^{-2}$

Constants

F	Faraday constant	$96484.56 \text{ A s mol}^{-1}$
R_u	Universal gas Constant	$8314.4 \text{ J kmol}^{-1} \text{K}^{-1}$

Indices

a	Anode
-----	-------

<i>c</i>	Cathode
<i>eff</i>	Effective
<i>i, j</i>	Chemical species

References

- [1] Ferguson, J. R., Fiard, J. M., Herbin, R., "Three-Dimensional Numerical Simulations for Various Geometries of Solid Oxide Fuel Cells", J. Power Sources, 58 (1996) 109-122.
- [2] Fiard, J. M., Herbin, R., "Comparison Between Finite Volume and Finite Element Methods for an Elliptic System Arising in Electrochemical Engineering", Comp. Methods in App. Mech. and Eng., 115, (1994) 315-338.
- [3] Haberman, B. A., Young, J. B., "Three-Dimensional Simulation of Chemically Reacting Gas Flows in the Porous Support Structure of an Integrated-Planar Solid Oxide Fuel Cell", Int. J. of Heat and Mass Transfer, 47, (2004) 3617-3629.
- [4] Khaleel, M. A., Lin, Z., Singh, P., Surdoval, W., Collin, D., "A finite element analysis modeling tool for solid oxide fuel cell development: coupled electrochemistry, thermal and flow analysis in MARC", J. of Power Sources, 130, (2004) 136-148.
- [5] Lehnert W., Meusinger J., Thom F., "Modelling of gas transport phenomena in SOFC anodes", J. Power Sources, 87, (2000) 57-63.
- [6] Li P. W., Chyu. M. K., "Simulation of the Chemical/Electrochemical Reaction and Heat/Mass Transfer for a Tubular SOFC Working in a Stack", J. Power Sources, 124, (2003) 487-498.
- [7] Chan, S. H., Khor, K. A., Xia, Z. T., "A complete polarization model of a solid oxide fuel cell and its sensitivity to the change of cell component thickness", J. Power Sources, 93, (2001) 130-140.
- [8] Campanari, S., Iora, P., J. Power Sources, "Definition and sensitivity analysis of a finite volume SOFC model for a tubular cell geometry", 132 (2004) 113-126.
- [9] Grujicic, M., Chittajallu, K. M., "Design and optimization of polymer electrolyte membrane (PEM) fuel cells", Applied Surface Sci., 227 (2004) 56-72.
- [10] Grujicic, M., and Chittajallu, K. M., "Optimization of the cathode geometry in polymer electrolyte membrane (PEM) fuel cells", Chem. Eng. Sci., 59 (2004) 5883-5895.

- [11] Anderson, W.K., Newman, J.C., Whitfield, D.L., Eric Nielsen, E.J., "Sensitivity Analysis for the Navier-Stokes Equations on Unstructured Meshes Using Complex Variables", AIAA Journal, 39, 1, (2001) 56-63.
- [12] Burden, R. L., Faires, D. J., "Numerical Analysis", Sixth Edition, Brooks/Cole Publishing Company, 1997, 16-26.
- [13] Secanell, M., Djilali, N., Suleman, A., "Optimization of a planar self-breathing PEM fuel cell cathode", AIAA 2006-6917, 11th AIAA/ISSMO Multidisciplinary Analysis and Optimization Conference, 6-8 Sept., 2006, Portsmouth, Virginia.
- [14] Huang, C. M., Shy, S. S., Lee, C. H., "On flow uniformity in various interconnects and its influence on cell performance of planar SOFC", J. Power Sources, 183, (2008) 205-213.
- [15] Lee, S., Jeong, H., Ahn, B., Lim, T., Son, Y., "Parametric study of the channel design at the bipolar plate in PEMFC performances", I. J. of Hydrogen Energy, 33, (2008) 5691-5696.
- [16] Anderson, W. K., Venkatakrisnan, V., "Aerodynamic Design Optimization on Unstructured Grids with a Continuous Adjoint Formulation", Computers and Fluids, 28, 4-5, (1999) 443-480.
- [17] Anderson, W. K., Bonhaus, D. L., "Airfoil Design on Unstructured Grids for Turbulent Flows", AIAA Journal, 37, 2, (1999) 185-191.
- [18] Burdyslaw, C. E., Anderson, W. K., "A General and Extensible Unstructured Mesh Adjoint Method", AIAA J. of Aerospace, Computing, Information, and Communication, 2, 10, 401-413 (2005).
- [19] Burdyslaw, C. E., "Achieving Automatic Concurrency Between Computational Field Solvers and Adjoint Sensitivity Codes," Ph.D. Thesis, University of Tennessee, Chattanooga, May, 2006.
- [20] Jameson, A., "Aerodynamic Design Via Control Theory", J. Scientific Computing, 3, (1998) 233-260.
- [21] Jameson, A., Alonso, J. J., Reuther, J., Martinelli, L., Vassberg, J. C., "Aerodynamic Shape Optimization Techniques Based on Control Theory", AIAA Paper No. 98-2538, (1998).
- [22] Mohammadi, B., "Optimal Shape Design, Reverse Mode of Automatic Differentiation and Turbulence", AIAA Paper No. 97-0099, (1997).

- [23] Nielsen, E. J., Anderson, W. K., "Recent Improvements in Aerodynamic Optimization on Unstructured Meshes", AIAA J., 40, 6, (2002) 1155-1163.
- [24] Nielsen, E. J., Anderson, W. K., "Aerodynamic Design Optimization On Unstructured Meshes Using the Navier-Stokes Equations", AIAA J., 37, 11, (1999) 1411-1419.
- [25] Nielsen, E. J., "Aerodynamic Design Sensitivities on an Unstructured Mesh Using the Navier-Stokes Equations and a Discrete Adjoint Formulation", Ph.D. Dissertation, Virginia Polytechnic Institute and State University, (1998).
- [26] Nielsen, E. J., Kleb, W. L., "Efficient Construction of Discrete Adjoint Operators on Unstructured Grids by Using Complex Variables", AIAA J., 44, 4 (2005) 827-836.
- [27] Park, M., "Adjoint-Based, Three-Dimensional Error Prediction and Grid Adaptation", AIAA Paper No. 2002-3286, (2002).
- [28] Kapadia S., Anderson W. K., Elliott L., Burdyslaw C., "Adjoint method for solid-oxide fuel cell simulations", J. Power Sources, 166 (2007) 376-385.
- [29] Kapadia S., Anderson W. K., Elliott L., Burdyslaw C., "Adjoint based Sensitivity Analysis and Error Correction Methods applied to Solid Oxide Fuel Cells", ASME J. Fuel Cell Sci. Tech., 6, 2, (2009).
- [30] Kapadia S., Anderson W. K., "Sensitivity Analysis for Solid Oxide Fuel cells using a Three-Dimensional Numerical Mode", J. Power Sources, 189 (2009) 1074-1082.
- [31] Kapadia S., Anderson W. K., Burdyslaw, C., "Channel shape optimization of solid oxide fuel cells using advanced numerical techniques", Computers and Fluids, 41, 1 (2011) 41-50.
- [32] Lin C., Huang L., Chiang L., Chyou Y., "Effects of clamping load on the thermal stress distribution in a planar SOFC with compressive sealing", ECS Transactions, 25, 2 (2009) 349-358.
- [33] Lin C., Huang L., Chiang L., Chyou Y., "Thermal stress analysis of planar solid oxide fuel cell stacks: Effects of sealing design", J. Power Sources 192 (2009) 515-524.
- [34] Chiang L., Liu H., Shiu Y., Lee C., Lee R., "Thermo-electrochemical and thermal stress analysis for an anode-supported SOFC cell", Renewable Energy 33 (2008) 2580-2588.
- [35] Iqbal G., Pakalapati S., Blancas F., Guo H., Celik I., Kang B., "PEN structure thermal stress analysis for planar-SOFC configurations under practical temperature field",

Advances in Materials Science for Environmental and Nuclear Technology II, Ceramic Transactions 227 (2011) 61-68.

[36] Jiang T., Chen T., "Thermal-stress analyses of an operating planar solid oxide fuel cell with the bonded compliant seal design", Int. J. Hydrogen Energy 34 (2009) 8223-8234.

[37] Weil K., Koeppel B., "Comparative finite element analysis of the stress-strain states in three different bonded solid oxide fuel cell seal designs", J. Power Sources 180 (2008) 343-353.

[38] Chiang L., Liu H, Shiu Y., Lee C., Lee R., "Thermal stress and thermo-electrochemical analysis of planar anode-supported solid oxide fuel cell: Effect of anode porosity", J. Power Sources 195 (2010) 1895-1904.

[39] ABAQUS webpage: <http://www.3ds.com/products/simulia/portfolio/abaqus/abaqus-portfolio/>

[40] FLUENT webpage:
<http://www.ansys.com/Products/Simulation+Technology/Fluid+Dynamics/Fluid+Dynamics+Products/ANSYS+Fluent>

[41] ANSYS webpage: <http://www.ansys.com>

[42] STAR-CD webpage: http://www.cd-adapco.com/products/star_cd/

[43] MARC webpage: <http://www.mscsoftware.com/product/marc>

[44] Wang, Y., Yoshiba, F., Watanbe, T., Weng, S., "Numerical analysis of electrochemical characteristics and heat/species transport for planar porous-electrode-supported SOFC", J. Power Sources, 170, (2007) 101-110.

[45] Hwang, J. J., Chen, C. K., Lai, D. Y., "Computational analysis of species transport and electrochemical characteristics of a MOLB-type SOFC", J. Power. Sources, 140, (2005) 235-242.

[46] Noren, D. A., Hoffman, M. A., "Clarifying the Butler-Volmer equation and related approximation for calculating activation losses in solid oxide fuel cell models", J. Power Sources, 152, (2005) 175-181.

[47] Costamagna, P., Selimovic, A., Borghi, M., Agnew, G., "Electrochemical model of the integrated planar solid oxide fuel cell (IP-SOFC)", Chem. Eng. J., 102, (2004) 61-69.

- [48] Saad, Y., Schultz, M. H., "GMRES: A Generalized Minimal Residual Algorithm for Solving Nonsymmetric Linear Systems", SIAM J. Sci. Stat. Comput., 7, (1986) 856-869
- [49] Grama A., Gupta, A., Karypis, G., Kumar, V., "Introduction to Parallel Computing", Second Edition, Addison Wesley, Jan. 16, 2003.
- [50] METIS webpage: <http://glaros.dtc.umn.edu/gkhome/views/metis>
- [51] POINTWISE webpage: <http://www.pointwise.com>
- [52] Roe, P. L., "Characteristic-based schemes for the Euler equations", Ann. Rev. Fluid Mech., 18, (1986) 337-365.
- [53] Busby M., "Steps Toward More Accurate and Efficient Simulations of Reactive Flows", Ph.D. Thesis, Mississippi State University, August 1997.